UNIVERSITÄT DUISBURG ESSEN

FH AACHEN UNIVERSITY OF APPLIED SCIENCES

The 3rd YRA MedTech Symposium is jointly organized by the FH Aachen and the University of Duisburg-Essen.

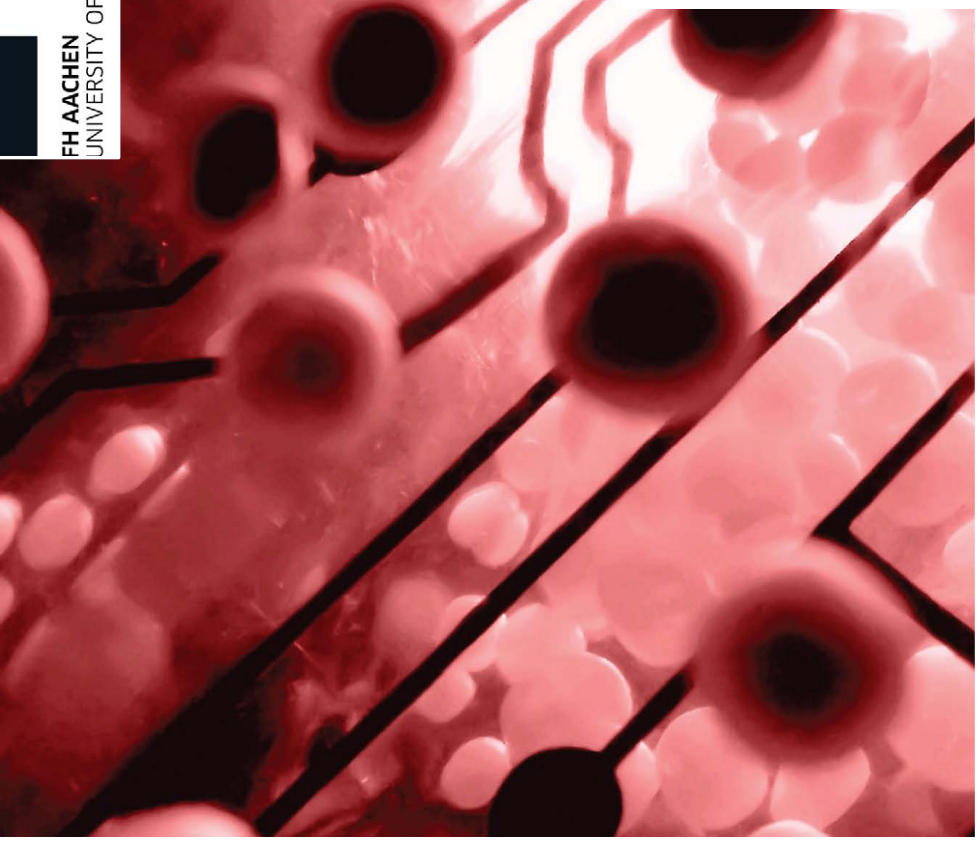

2019

Symposium Proceedings

Editors:
Manfred Staat
Daniel Erni

YRA – Young Researchers Academy MedTech in NRW

Ph.D., Master, and Bachelor students of all universities in NRW (Uni & FH) working in areas related to biomedical engineering are kindly invited to present their research or their thesis at the

3rd YRA MedTech Symposium

May 24 / 2019 / FH Aachen

FH Aachen / Campus Jülich
Heinrich-Mußmann-Str. 1
52428 Jülich

http://www.yra-medtech.de/

Foreword

This is already the third YRA MedTech Symposium with the active participation of colleagues from several universities and a considerable number of Ph.D., master and bachelor students. The first symposium took place in Duisburg in 2016, the second was organized parallel to the IEEE Workshop / Sensorica 2017 in Mühlheim an der Ruhr. As with all experiments, the format was varied slightly each time. But the basic concept, to provide an open platform for bachelor, master, and doctoral students to present either their research or their final thesis in the realm of biomedical engineering or in related fields such as e.g. (non-exhaustive):

- Biomechanics, Implants, Biofluidmechanics, Microfluidics, ...
- Bioinformatics, Telemedicine, AAL, Hospital Engineering, ...
- Bioelectromagnetics, Bioelectronics, Biophysics, Medical Physics, ...
- Medical Imaging, Biosensors, Lab-on-a-Chip, ...
- Numerical Modeling, HPC, Multi-Scale Approaches, ...

has proven itself and remained unchanged.

This open list of topics shows how versatile but also strongly interdisciplinary biomedical engineering is. This requires openness to initially foreign topics and methods. As a side effect, colleagues from universities with very different backgrounds got to know each other and exchanged ideas, established new contacts and deepened existing ones. Some colleagues from other universities found interest and took part. Methods which were presented in one or the other lecture could be integrated into the own research by another colleague.

In some cases, students of biomedical engineering are also involved right from the start. They first presented their bachelor's or master's theses and now, in their role as doctoral students, support the next generation of students in their final theses.

We would like to thank all those who have contributed to this success in the past, those who actively participated this year and those who are already considering what they would like to contribute next time.

Manfred Staat Daniel Erni

May 24, 2019.

Agenda – YRA MedTech Symposium 2019

Time / Room		Lecture Room: Campus Jülich, Hörsaal 00H01
Start	**End**	
9:00 Gerling Pavillon	9:30	**Registration**
9:30 Hörsaal 00H01	9:40	**Opening and Welcome** Prof. Dr. Manfred Staat (Symposium Chair), Prof. Dr. Christof Schelthoff (Dean)
9:40 Hörsaal 00H01 **Tissue Engineering Measurements Modeling and Simulations** Chair: Prof. I. Digel	11:00	**9:40 – 10:00** **Treating arterial hypertension in a cell culture well** Robin Bayer[1,2], Jürgen Hescheler[1], Gerhard Artmann[1,2], and Aysegül Artmann[2] [1] Institute for Neurophysiology, University of Cologne, D-50931 Köln, Germany [2] Institute for Bioengineering, Faculty of Medical Engineering and Technomathematics, FH Aachen University of Applied Sciences, D-52428 Jülich, Germany
		10:00-10:20 **Development of a tool to analyze the conduction speed in microelectrode array measurements of cardiac tissue** Jan Hunker[1], Alexander Jung[1], Matthias Goßmann[2], Peter Linder[2], and Manfred Staat[1] [1] Institute for Bioengineering, Faculty of Medical Engineering and Technomathematics, FH Aachen University of Applied Sciences, D-52428 Jülich, Germany [2] innoVitro GmbH, Artilleriestr. 2, D-52428 Jülich, Germany
		10:20 – 10:40 **Characterization of horse-derived induced pluripotent stem cells** Vanessa Bröker[1], Dorothee Hielscher[1], Andreas Pansky[1], Kurt Pfannkuche[2], and Edda Tobiasch[1] [1] Stem Cell Laboratory, Department of Natural Sciences, Bonn-Rhine-Sieg University of Applied Sciences, D-53359 Rheinbach, Germany [2] Laboratory for Cardiac Tissue Engineering, Center for Physiology and Pathophysiology, University of Cologne, D-50931 Cologne, Germany
		10:40 – 11:00 **Modification of a computer model of human stem cell-derived cardiomyocyte electrophysiology based on Patch-Clamp measurements** Aravind Hariharan Raman[1], Alexander Jung[1], András Horváth[2], Nadine Becker[2], and Manfred Staat[1] [1] Institute for Bioengineering, Faculty of Medical Engineering and Technomathematics, FH Aachen University of Applied Sciences, D-52428 Jülich, Germany [2] Nanion Technologies GmbH, Ganghoferstr. 70A, D-80339 Munich, Germany
11:00 Gerling Pavillon	11:20	**Coffee Break / Networking with other Experts**
11:20 Hörsaal 00H01 **Brain and Neurological Computer Interface** Chair: Prof. K. Ziemons		**11:20 – 11:40** **Feature extraction and classification of motor imagery EEG signals for brain computer interface controlled electromechanical implants** Nikolas P. Klein[1], Adrian Niemann[1], and Klaus Brinker[1] [1] Hamm-Lippstadt University of Applied Sciences, Marker Allee 76-78, D-59063 Hamm, Germany
		11:40 – 12:00 **Improvements in classification accuracy of a pre-existing P300-speller system** Adrian Niemann[1], and Klaus Brinker[1] [1] Hamm-Lippstadt University of Applied Sciences, Marker Allee 76-78, D-59063 Hamm, Germany
		12:00 –12:20 **A hardware efficient implementation of a spike detection algorithm in neural closed-loop-systems** Andreas Erbslöh[1], Roman Burkard[1], Reinhard Viga[1], Rainer Kokozinski[1,2] [1] Institute of Electronic Components and Circuits, Faculty of Engineering, University of Duisburg-Essen, D-47057 Duisburg, Germany [2] Fraunhofer Institute of Microelectronic Circuit and Systems, D-47057 Duisburg, Germany

Agenda – YRA MedTech Symposium 2019

		12:40	**12:20 – 12:40** **Bayesian multi-level model to inspect relationship between socioeconomic status and subjective health in 10,000 social brain** Nathania Suryoputri[1], and Danilo Bzdok[2] [1] Institute for Bioengineering, Faculty of Medical Engineering and Technomathematics, FH Aachen University of Applied Sciences, D-52428 Jülich, Germany [2] Department of Psychiatry, Psychotherapy and Psychosomatics, RWTH Aachen University, D-52072 Aachen, Germany
			Poster **Listening effort and cognitive functions in cochlear implant users** Khaled Abdellatif[1], Stefan Schreitmüller[2], Martin Walger[2], and Hartmut Meister[1] [1] Jean Uhrmacher Institute for Clinical ENT-Research, University of Cologne, D-50931 Cologne, Germany [2] Clinic of Otorhinolaryngology, Head and Neck Surgery, University of Cologne, D-50931 Cologne, Germany
12:40 Gerling Pavillon		13:50	**Lunch Break and Poster Session**
13:50 Hörsaal 00H01 **MRI and Tomography** Chair: Prof. J. Trzewik			**13:50 – 14:10** **Continuous measurement methods for non-invasive determination of bladder volume** Romina Möllmann[1], Walid Albanna[2], Anne Benninghaus[3], and Konstantin Kotliar[1] [1] Fraunhofer Institute for Microelectronic Circuits and Systems IMS, D-47057 Duisburg, Germany [2] Alexianer GmbH Krefeld, Clinic for Gerontopsychiatry and Psychotherapy, D-47805 Krefeld, Germany [3] University of Duisburg-Essen, Department of Electronic Components and Circuits, D-47057 Duisburg, Germany
			14:10 – 14:30 **Design and characterization of metamaterial-based zeroth-order resonance antennas for 3T MRI** Muhamed Dedic[1], Jan Taro Svejda[1], Andreas Rennings[1], and Daniel Erni[1] [1] General and Theoretical Electrical Engineering (ATE), Faculty of Engineering, University of Duisburg-Essen, and CENIDE, Center for Nanointegration Duisburg-Essen, D-47048 Duisburg, Germany
			14:30 – 14:50 **The influence of CT tube current and voltage on extended Hounsfield unit values** Zehra Ese[1,2], Daniel Erni[1], and Waldemar Zylka[2] [1] General and Theoretical Electrical Engineering (ATE), Faculty of Engineering, University of Duisburg-Essen, and CENIDE, Center for Nanointegration Duisburg-Essen, D-47048 Duisburg, Germany [2] Faculty of Electrical Engineering and Applied Natural Sciences, Westphalian University, Campus Gelsenkirchen, D-45897 Gelsenkirchen, Germany
			14:50 – 15:10 **Design and first results of a phantom study on the suitability of iterative reconstruction for lung-cancer screening with low-dose computer tomography** Britta König[1,4], Nika Guberina[2], Hilmar Kühl[1,3], and Waldemar Zylka[4] [1] Faculty of Medicine, University of Duisburg-Essen, D-47057 Duisburg, Germany [2] Institute for Diagnostic and Interventional Radiology and Neuroradiology, University Hospital Essen, D-45122 Essen, Germany [3] Clinic for Radiology, St. Bernhard-Hospital Kamp-Lintfort GmbH, D-47475 Kamp-Lintfort, Germany [4] Faculty of Electrical Engineering and Applied Natural Sciences, Westphalian University, Campus Gelsenkirchen, D-45897 Gelsenkirchen, Germany
			15:10 – 15:30 **Establishment of a 4-Alternative-Forced-Choice test to evaluate the radiological performance of iterative reconstruction in computer tomography images** Hoai Thu Nguyen[1], Britta König[1,2], and Waldemar Zylka[1] [1] Faculty of Electrical Engineering and Applied Natural Sciences, Westphalian University, Campus Gelsenkirchen, D-45897 Gelsenkirchen, Germany [2] Faculty of Medicine, University of Duisburg-Essen, D-47057 Duisburg, Germany

Agenda – YRA MedTech Symposium 2019

		15:50	**15:30 – 15:50** **Numerical evaluation of small animal warming potential when using a birdcage coil for 7T magnetic resonance imaging** Maíra M. Garcia [1,2], Tiago R. Oliveira[3], Daniel Papoti[3], Khallil Chaim[4], Daniel Erni[2], and Waldemar Zylka[1] [1] Faculty of Electrical Engineering and Applied Natural Sciences, Westphalian University, Campus Gelsenkirchen, D-45897 Gelsenkirchen, Germany [2] General and Theoretical Electrical Engineering (ATE), Faculty of Engineering, University of Duisburg-Essen, and CENIDE – Center for Nanointegration Duisburg-Essen, D-47048 Duisburg, Germany [3] Department of Biomedical Engineering, Federal University of ABC, 09606-070 São Bernardo do Campo, Brazil [4] Department and Institute of Radiology, University of São Paulo, 05403-010 São Paulo, Brazil
	15:50 Gerling Pavillon	16:10	**Coffee Break / Networking with other Experts**
	16:10 Hörsaal 00H01 **Optical Analyses and Sensoring** Chair: Prof. W. Zylka	17:30	**16:10 – 16:30** **Recognition of subjects with mild cognitive impairment (MCI) by the use of retinal arterial vessels magnetic resonance imaging** Jonas Zingsheim[1], Timo Grimmer[2], Marion Ortner[2], Christoph Schmaderer[3], Christine Hauser[3], and Konstantin Kotliar[1] [1] Faculty of Medical Engineering and Technomathematics, FH Aachen University of Applied Sciences, D-52428 Jülich, Germany [2] Department of Psychiatry and Psychotherapy, Technische Universität München, D-80333 München, Germany [3] Department of Nephrology, Technische Universität München, D-80333 München, Germany **16:30 – 16:50** **Vasomotion in retinal vessels of patients presenting post hemorrhagic hydrocephalus following subarachnoid hemorrhage** Yannik Blum[1], Walid Albanna[2], Anne Benninghaus[3], and Konstantin Kotliar[1] [1] Institute for Bioengineering, Faculty of Medical Engineering and Technomathematics, FH Aachen University of Applied Sciences, D-52428 Jülich, Germany [2] Department of Neurosurgery, RWTH Aachen University, D-52074 Aachen, Germany [3] Chair of Medical Engineering, Helmholtz-Institute for Biomedical Engineering, RWTH Aachen, D-52074 Aachen, Germany **16:50 – 17:10** **Utilization of fluorescence spectroscopy and neural networks in clinical analysis** Fouad Azar[1], and Ilya Digel[1] [1] Institute for Bioengineering, Faculty of Medical Engineering and Technomathematics, FH Aachen University of Applied Sciences, D-52428 Jülich, Germany **17:10 – 17:30** **Development of a camera-based pulse oxymeter for neonatal intensive care units** Rene Thull[1], Christian Schiffer[1], and Andreas Diewald[1] [1] Labor für Radartechnologie und optische Systeme (LaROS), Faculty of Electrical Engineering, Trier University of Applied Sciences, D-54293 Trier, Germany
	17:30 Hörsaal 00H01	17:30	**Session Change**
	17:30 Hörsaal 00H01 **Application of Physical Methods** Chair: Prof. K. Kotliar	18:10	**17:30 – 17:50** **Approach for erosion processes at HF-surgery devices** Tino Morgenstern[1], Manuel Lange[1], Stephan Klöckner[2], and Jörg Himmel[1] [1] Institute for measurement and sensor technology, Hochschule Ruhr West, D-45479 Mülheim an der Ruhr, Germany [2] Olympus Surgical Technologies Europe, D-22045 Hamburg, Germany **17:50 – 18:10** **Diamond like carbon as a hydrophobic material for electrowetting** Semih Türk[1], Reinhard Viga[1], and Holger Vogt[2] [1] Electronic Components and Circuits, Department of Electrical Engineering and Information Technology, University of Duisburg-Essen, D-47057 Duisburg, Germany [2] CMOS Microsystem Technologies, Fraunhofer Institute for Microelectronic Circuits and Systems, D-47057 Duisburg, Germany
	18:10 Hörsaal 00H01	18:10	**Closing Remarks**

Session Tissue Engineering Measurements Modeling and Simulations

Treating arterial hypertension in a cell culture well

Robin Bayer[(1)(2)], Jürgen Hescheler[(1)], Gerhard Artmann[(1)(2)], and Aysegül Artmann[(2)]

[(1)] Institute for Neurophysiology,
University of Cologne,
D-50931 Köln, Germany

[(2)] Institute for Bioengineering, Faculty of Medical Engineering and Technomathematics,
FH Aachen University of Applied Sciences,
D-52428 Aachen, Germany

Email.: bayer@fh-aachen.de
Web.: https://www.fh-aachen.de/en/research/institute-for-bioengineering/

Hypertension describes the pathological increase of blood pressure, which is most commonly associated with the increase of vascular wall stiffness [1]. Referring to the "Deutsche Bluthochdruck Liga" this pathology shows a growing trend in our aging society. In order to find novel pharmacological and probably personalized treatments, we want to present a functional approach to study biomechanical properties of a human aortic vascular model.

In this method review we will give an overview of recent studies which were carried out with the CellDrum technology [2] and underline the added value to already existing standard procedures known from the field of physiology.

Herein described CellDrum technology is a system to measure functional mechanical properties of cell monolayers and thin tissue constructs in-vitro. Additionally, the CellDrum enables to elucidate the mechanical response of cells to pharmacological drugs, toxins and vasoactive agents. Due to its highly flexible polymer support, cells can also be mechanically stimulated by steady and cyclic biaxial stretching.

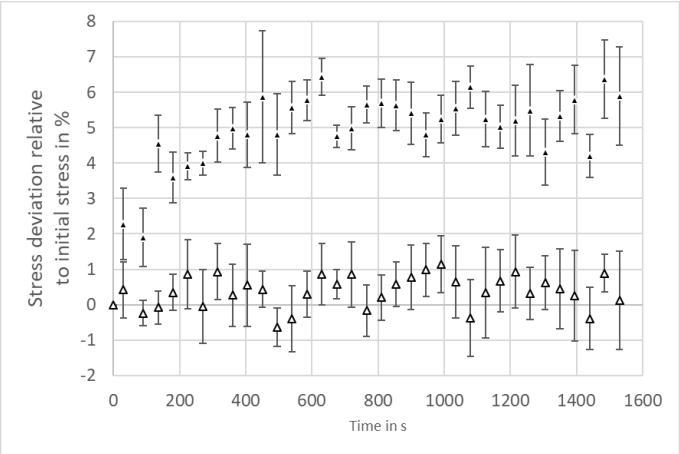

Table 1: Biomechanical analysis of vasoactive agents carried out with CellDrum system. 1.5x10^5 human aortic smooth muscle cells (haSMC) were cultured on functionalized CellDrum membrane. Endothelin 1 (ET1) was added to the cell culture media in a final concentration of 100nM. The same amount of ET1 solvent was added to the control group. The biomechanical effect was observed as progression over time. The graph shows the mean values of six biological replicas which were normalized and converted to percentage to their initial stress. Error bars indicating SEM.

ET1 increases the mechanical stress to 5,4 ± 0,6% to initial tension, whereas the control was increased to 0,4 ± 0,4%.

The PulSElect system was developed to expose CellDrum-Cell-Models to a brought range of precise and defined dose of mechanical stimulation. Due to its high dynamic functional principle, the cells can be exposed to various, highly customized pressure pulses, resulting in cellular stretching and or compression [3].

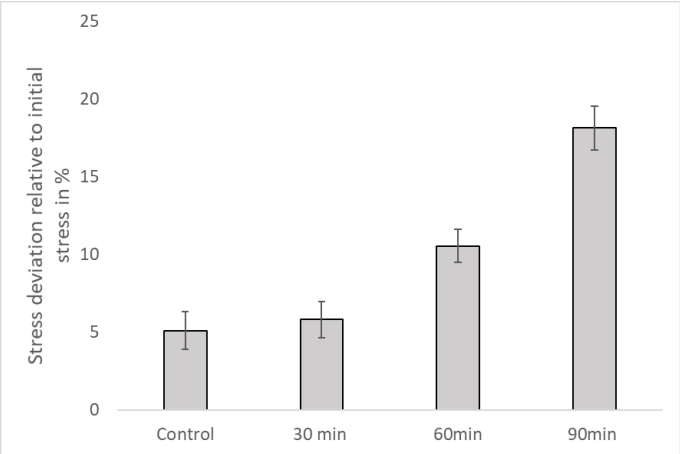

Table 2: haSMC model was exposed to mechanical stimulation via PulSElect system. A negative Gaussian pulse wave with a stimulation frequency of 2Hz was chosen. Different stimulation intervals were tested ranging from 0 to 90 minutes. The training sequence was carried out three times over two days. Mechanical properties of the cells were evaluated by comparing mechanical measurements before and after cell stimulation. The measurement was carried out with six biological and five technical replicas.

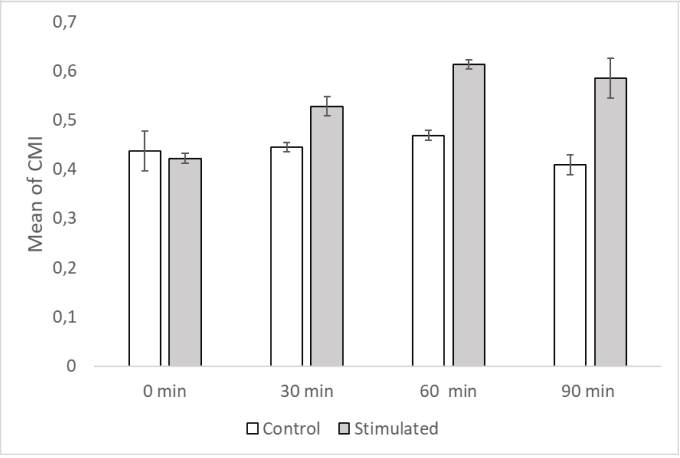

Table 3: Evaluation of cytoskeletal alignment affected by mechanical stimulation. Angle dependent frequency analysis of Phalloidin488 stained F-Actin structures was carried out by an in house made LabVIEW software.
An equivalent mechanical stimulation protocol to Table 2 was used. The bars representing three pooled biological replicas from which 90 analyses have been made each. Error bars indicating SEM.
CMI expresses cytoskeletal alignment numerically. Higher values indication higher structural alignment.
Comparing mech. unstimulated and stimulated specimen, the F-Actin alignment increases according to the stimulation duration.

Due to these technologies, we gained various results, which show correlation between cytoskeletal distribution, gene expression and functional biomechanical analysis of a human aortic smooth muscle cell monolayer model. These data indicating a promising progression of the technology, which might lead in near future to high efficient and personalized medication dose adjustment in combination with nowadays stem cell research.

This study gives a brief impression and an insight in current applications of the CellDrum technology of the Institute for Bioengineering, FH Aachen, Jülich, Germany, with its challenging perspectives towards further medical and scientific applications [4].

References

[1] R. M. Touyz *et al.*, “Vascular smooth muscle contraction in hypertension,” *Cardiovasc. Res.*, vol. 114, no. 4, pp. 529–539, 2018.

[2] G. M. Artmann, J. Hescheler, H. Meruvu, S. Kizildag and A. Temiz-Artmann, “Biological, Physical and Technical Basics of Cell Engineering,” In: G.M. Artmann, A. Artmann, A.A. Zhubanova, I. Digel (eds.) *Biological, Physical and Technical Basics of Cell Engineering*, Singapore: Springer, pp. 157-192, 2018.

[3] R. Bayer, T. Creutz, G. Artmann, A. T. Artmann and J. Hescheler, “The CellDrum and PulSElect system : tools to evaluate mechanical and pharmacological effects on arterial cells,” 52*nd Annual Conference of the German Society for Biomedical Engineering*. September 26-28, Aachen, Germany, *Poster,* 2018.

[4] G. Artmann et al., "CellDrum electrode arrangement for measuring mechanical stress," Patent WO2017121890, July 20, 2017.

Development of a tool to analyze the conduction speed in microelectrode array measurements of cardiac tissue

Jan Hunker[(1)], Alexander Jung[(1)], Matthias Goßmann[(2)], Peter Linder[(2)], and Manfred Staat[(1)]

[(1)] Institute for Bioengineering, Faculty of Medical Engineering and Technomathematics, FH Aachen University of Applied Sciences, D-52428 Jülich, Germany

[(2)] innoVitro GmbH, Artilleriestr. 2, D-52428 Jülich, Germany

E-Mail: jan.hunker@alumni.fh-aachen.de
Web: www.ifb.fh-aachen.de

Abstract – The discovery of human induced pluripotent stem cells reprogrammed from somatic cells [1] and their ability to differentiate into cardiomyocytes (hiPSC-CMs) has provided a robust platform for drug screening [2]. Drug screenings are essential in the development of new components, particularly for evaluating the potential of drugs to induce life-threatening pro-arrhythmias. Between 1988 and 2009, 14 drugs have been removed from the market for this reason [3]. The microelectrode array (MEA) technique is a robust tool for drug screening as it detects the field potentials (FPs) for the entire cell culture. Furthermore, the propagation of the field potential can be examined on an electrode basis. To analyze MEA measurements in detail, we have developed an open-source tool.

This tool is Python-based (version 2.7.1.5) and takes the activation time and latency of every heartbeat as input. Based on the activation times and latencies, it computes the heartbeat rate, the heartbeat interval, and the linear conduction speed of the FP wave front (between the electrodes detecting minimum and maximum activation time). Furthermore, it computes the local conduction velocities at each electrode via the finite difference method [4]. The results of each quantity are stored in a list, histograms, scatter plots, box-plots, and quiver-plots (conduction velocity at each electrode). The tool also provides statistical analyses for a given set of heartbeats. This can be useful for instance for dose-response studies in drug screenings. When evaluating linear conduction speeds with this tool, however, the user needs to consider the shape of the FP wave front: the FP wave front needs at least to be approximately circular for the linear conduction speed to be a useful measure. We found that the use of an electrode-distance threshold works well to filter out heartbeats with a non-circular FP wave. In particular, the distance between the electrodes detecting minimum and maximum activation times is evaluated and if it is below a certain threshold, the given data set is not considered for further analysis. Comprehensive studies revealed that the threshold value should be at least 75% of the maximum electrode distance of the given MEA. Furthermore, a threshold for the heartbeat rate and the heartbeat interval can be selected in order to exclude outliers caused by measurement inaccuracies. However, this threshold should be set carefully when investigating diseases and drug response. A detailed examination of the FP at given electrodes is necessary to guarantee that extreme values are not caused by pro-arrhythmic events. The information on analyzed and rejected beats is always stored in the result-list.

The tool was validated by comparing its outcome with the outcome of a commercially available tool (Cardio 2D$^+$, Multi Channel Systems MCS, Germany) for a given set of data. The data contained measurements for a dose response study of the drug E-4031 on hiPSC-CMs and was provided by MCS (Dr. Thomas Mayer, MCS). In the given study hiPSC-CMs of cell type Cor.4U (manufactured by Ncardia) were used. Electrodes in the MEAs are arranged in an 8x8-matrix with an equal electrode spacing of 1000 µm. Five samples were tested; the measurement time was 120 seconds each. One of the samples was used for the control and each of the four others was treated with the drug (10

nM, 30 nM, 100 nM, 300 nM). E-4031 is an anti-arrhythmic drug that blocks the potassium channels and thus influences repolarization. However, the blockage of the rapid-delayed rectifier current may lead to severe pro-arrhythmias by prolonging the QT interval [5]. The box plot in Fig. 1 shows the distribution of heartbeat rates. The heartbeat rates decrease with increasing doses of E-4031 treatments. This is associated with a prolonged repolarization phase. The outcome is in line with the outcome of the commercial software Cardio2D$^+$. However, it has some advantages over Cardio2D$^+$, e.g. the threshold function to filter data, and a more comprehensive statistical analysis including quiver-plots. Therefore, it will be utilized in various electrophysiological studies in the future.

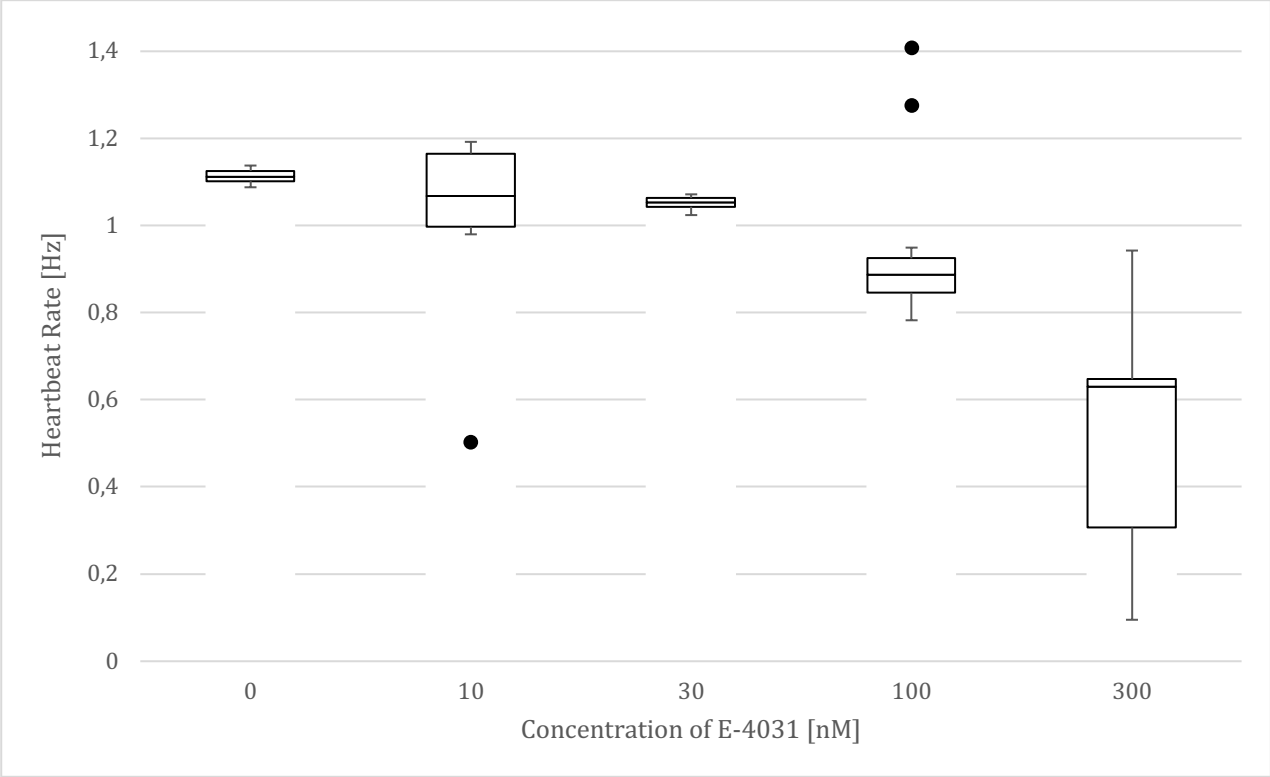

Figure 1: Heartbeat rate as a function of drug concentration of E-4031. Median values, first quartiles, third quartiles are visualized by a Whisker-Boxplot. Error bars represent the Whiskers (length max. 1.5 IQR). Dots represent the outliers. The outliers (147,1 and 666,7 Hz) at 300 nM exceed the scale. Nmber of heartbeats in 120 sec. was n=132 (0 nM), n=127 (10 nM), n=125 (30 nM), n=105 (100 nM), and n=49 (300 nM).

Acknowledgment: Supported by the German Federal Ministry of Education and Research through the KMU-innovativ program, grant 02P18K021.

References

[1] K. Takahashi, K. Tanabe, M. Ohnuki, M. Narita, T. Ichisaka, K. Tomoda and S. Yamanaka, "Induction of pluripotent stem cells from adult human fibroblasts by defined factors," *Cell*, vol. 131, no. 5, pp. 861-872, November 2007.

[2] K. Blinova, Q. Dang, D. Millard, G. Smith, J. Pierson, L. Guo, M. Brock, H.R. Lu, U. Kraushaar, H. Zeng, H. Shi, X. Zhang, K. Sawada, T. Osada, Y. Kanda, Y. Sekino, L. Pang, T.K. Feaster, R. Kettenhofen, N. Stockbridge, D.G. Strauss and G. Gintant, "International multisite study of human-induced pluripotent stem cell-derived cardiomyocytes for drug proarrhythmic potential assessment," *Cell Reports*, vol. 24, no. 13, pp. 3582-3592, September 2018.

[3] K. Blinova, J. Stohlman, J. Vicente, D. Chan, L. Johannesen, M.P. Hortigon-Vinagre, V. Zamora, G. Smith, W.J. Crumb, L. Pang, B. Lyn-Cook, J. Ross, M. Brock, S. Chvatal, D. Millard, L. Galeotti, N. Stockbridge and D.G. Strauss, "Comprehensive translational assessment of human-induced pluripotent stem cell derived cardiomyocytes for evaluating drug-induced arrhythmias," *Toxicol. Sci*., vol. 155, no. 1, pp. 234-247, January 2017.

[4] C.D. Cantwell, C.H. Roney, F.S. Ng, J.H. Siggers, S.J. Sherwin and N.S. Peters, "Techniques for automated local activation time annotation and conduction velocity estimation in cardiac mapping," *Comput. Biol. Med*., vol. 65, pp. 229-242, October 2015.

[5] C. Luo, K. Wang and H. Zhang, "Modelling the effects of quinidine, disopyramide, and E-4031 on short QT syndrome variant 3 in the human ventricles," *Physiol. Meas*., vol. 38, no. 10, pp. 1859-1873, September 2017.

Characterization of horse-derived induced pluripotent stem cells

Vanessa Bröker[(1)], Dorothee Hielscher[(1)], Andreas Pansky[(1)], Kurt Pfannkuche[(2)], and Edda Tobiasch[(1)]

[(1)] Stem Cell Laboratory,
Department of Natural Sciences, Bonn-Rhine-Sieg University of Applied Sciences,
D-53359 Rheinbach, Germany

[(2)] Laboratory for Cardiac Tissue Engineering,
Center for Physiology and Pathophysiology, University of Cologne,
D-50931 Cologne, Germany

E-Mail: edda.tobiasch@h-brs.de
Web: https://www.h-brs.de/de/prof-dr-edda-tobiasch

Abstract – Horse racing is a passionate and extremely costly business. Injuries, especially bone fractures, in these valuable animals could potentially lead to career-ending and even life-ending fate because treatments are limited due to lack of bone grafts [1]. A novel promising alternative implies the application of stem cell-based therapies, notably the use of induced pluripotent stem cells (iPSC) from the same horse, which greatly reduce the issue of immune rejection and presumably reduce the time period for recovery [2].
The aim of this study was to characterize horse skin fibroblast-derived iPSCs and to compare them to human fibroblast-derived iPSCs. Since the equine gene sequences of the pluripotency markers, namely Oct4, Sox2, c-Myc and Klf4 are still unknown, alignments of predicted sequences from different species were performed to design the predicted respective primers for RT-PCR. Additionally, immunofluorescence staining for the pluripotency markers was performed. Another interesting aspect for characterization of iPSCs are purinergic receptors, which are divided into seven ion-gated P2X and eight G-protein coupled P2Y receptors [3], [4]. Similarly, the gene sequences are only predicted in horse and primer design was performed accordingly to those of the pluripotency markers.
The morphology of the equine compared to the human iPSCs is similar, however, equine iPSCs form a more roundish structure and denser embryoid bodies. The predicted RT-PCR primer sequences for the pluripotency markers successfully amplified the respective genes. Among these genes, expression of Sox2 was confirmed on protein level by immunofluorescence with human and equine iPSCs showing a similar expression. Contrary to mesenchymal stem cells [5], only few purinergic receptors are expressed in human iPSCs. Preliminary data suggests that the designed primer amplified P2Y2 in equine iPSCs. The prospective outcome could possibly help to establish stem cell-based therapies which might provide a faster and easier fracture healing in horses, especially racing horses.

References

[1] J. A. Auer and D. W. Grainger, “Fracture management in horses: Where have we been and where are we going?,” *Vet. J.*, vol. 206, no. 1, pp. 5–14, Oct. 2015.

[2] K. Takahashi and S. Yamanaka, “Induction of pluripotent stem cells from mouse embryonic and adult fibroblast cultures by defined factors,” *Cell*, vol. 126, no. 4, pp. 663–676, 2006.

[3] Y. Zhang and E. Tobiasch, “The role of purinergic receptors in stem cells and their consecutive tissues,” in *Adult progenitor cell standardization*, P. Di Nardo, Ed. Aalborg: River Publisher, 2011, pp. 73–92.

[4] P. F. Ottensmeyer, M. Witzler, M. Schulze and E. Tobiasch, “Small molecules enhance scaffold-based bone grafts via purinergic receptor signaling in stem cells.,” *Int. J. Mol. Sci.*, vol. 19, no. 11, article 3601, Nov. 2018.

[5] N. Zippel *et al.*, “Purinergic receptors influence the differentiation of human mesenchymal stem cells,” *Stem Cells Dev.*, vol. 21, no. 6, pp. 884–900, Apr. 2012.

Modification of a computer model of human stem cell-derived cardiomyocyte electrophysiology based on Patch-Clamp measurements

Aravind Hariharan Raman[(1)], Alexander Jung[(1)], András Horváth[(2)], Nadine Becker[(2)], and Manfred Staat[(1)]

[(1)] Institute for Bioengineering, Faculty of Medical Engineering and Technomathematics,
FH Aachen University of Applied Sciences,
D-52428 Jülich, Germany

[(2)] Nanion Technologies GmbH,
Ganghoferstr. 70A,
D-80339 Munich, Germany

E-Mail: raman@fh-aachen.de
Web: www.ifb.fh-aachen.de

Abstract – Human induced pluripotent stem cells (hiPSCs) have shown to be promising in disease studies and drug screenings [1]. Cardiomyocytes derived from hiPSCs have been extensively investigated using patch-clamping and optical methods to compare their electromechanical behaviour relative to fully matured adult cells. Mathematical models can be used for translating findings on hiPSC-CMs to adult cells [2] or to better understand the mechanisms of various ion channels when a drug is applied [3,4]. Paci *et al*. (2013) [3] developed the first model of hiPSC-CMs, which they later refined based on new data [3]. The model is based on iCells® (Fujifilm Cellular Dynamics, Inc. (FCDI), Madison WI, USA) but major differences among several cell lines and even within a single cell line have been found and motivate an approach for creating sample-specific models. We have developed an optimisation algorithm that parameterises the conductances (in S/F=Siemens/Farad) of the latest Paci *et al*. model (2018) [5] using current-voltage data obtained in individual patch-clamp experiments derived from an automated patch clamp system (Patchliner, Nanion Technologies GmbH, Munich).

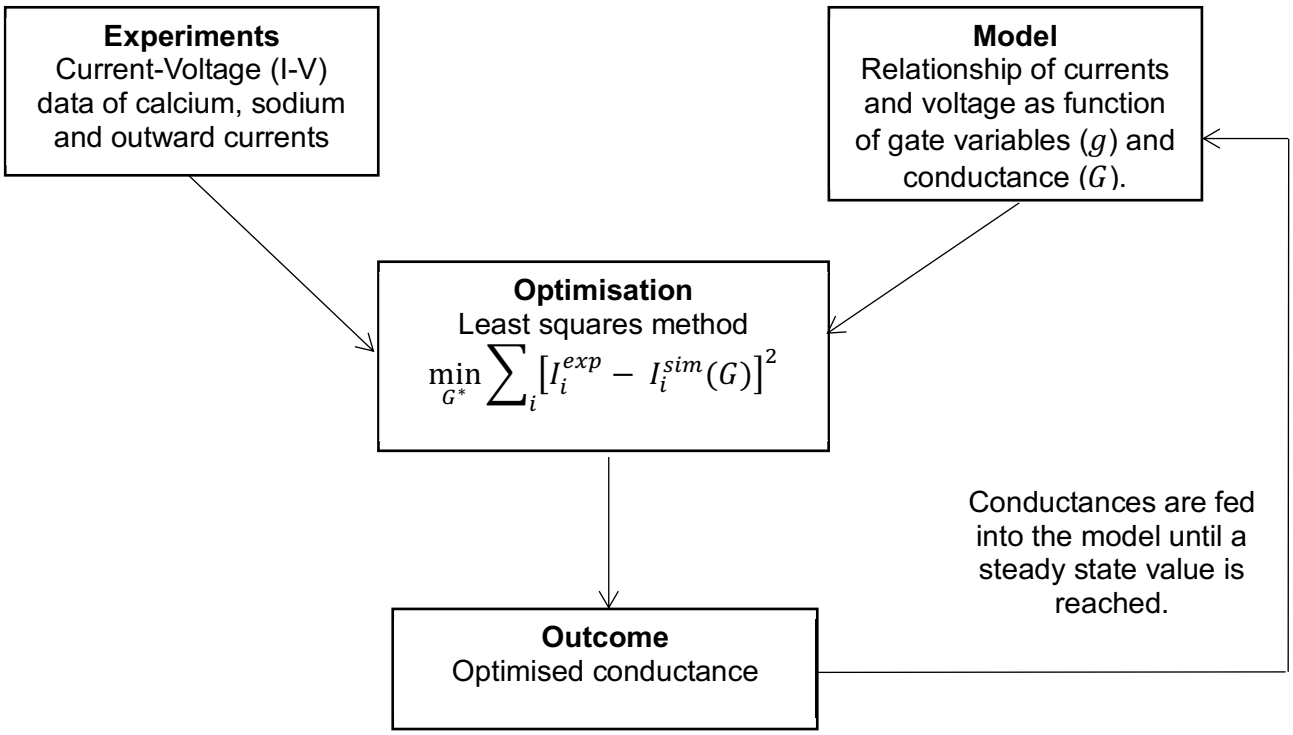

Fig.1: The flowchart of the optimisation scheme.

Methods: The flowchart of the optimization algorithm is shown in Fig. 1; the Python library SciPy is used. In brief, the algebraic equations and the initial value problem of the differential equations of the latest Paci model [5] and experimental current-voltage data are taken as input. Then, the conductance of the model are optimised by a least squares procedure in such a way that the model outcome fits the experimental data best. This is done iteratively until steady state of the conductance of the ion channels is achieved. Here, artificial data was generated to validate the algorithm by randomly scaling conductance of the sodium and calcium channels of the latest Paci model [5] (factors were between 1.2 and 1.5).

Table.1: Performance of optimisation algorithm. True conductance represents the conductance of the scaled model that generates the artificial data; optimised conductance is the outcome of the algorithm. Furthermore, the error is given.

Ion Channel	True Conductance (S/F)	Optimised Conductance (S/F)	Error (%)
I_{Na}	5506.84	5982.64	8.64
I_{CaL}	10.39	8.98	13.57
I_{bNa}	1.88	2.10	11.02
I_{bCa}	1.02	1.14	12.30
I_{NaL}	22.43	20.53	8.46

Results and discussions: The optimised conductances are in good agreement with the true conductances; the maximum relative error was 14%. When using experimental data, some shape differences in the computed and measured current-voltage curves have been found [4], which were suggested to be attributed to different ion channel kinetics. Therefore, our next aim is to integrate the ion channel kinetics, which is represented by the equations for the gap variables, into the optimisation algorithm.

Acknowledgment: Supported by the German Federal Ministry of Education and Research through the KMU-innovativ program, grant 02P18K021.

References

[1] K. Blinova, Q. Dang, D. Millard, *et al*., "International multisite study of human-induced pluripotent stem cell-derived cardiomyocytes for drug proarrhythmic potential assessment," *Cell Reports*, vol. 24, no. 13, pp. 3582-3592, Sept. 2018.

[2] A. Tveito, K. H. Jæger, N. Huebsch, *et al.* "Inversion and computational maturation of drug response using human stem cell derived cardiomyocytes in microphysiological systems," *Sci. Rep.*, vol. 8, no. 1, article 17626, Dec. 2018.

[3] Paci, M., Hyttinen, J., Aalto-Setälä, K. *et al.* "Computational models of ventricular- and atrial-like human induced pluripotent stem cell derived cardiomyocytes," *Ann. Biomed. Eng.*, vol. 41, no. 11, pp 2334-2348, 2013.

[4] C. L. Lei, K. Wang, M. Clerx, *et al.* "Tailoring mathematical models to stem-cell derived cardiomyocyte lines can improve predictions of drug-induced changes to their electrophysiology," *Front. Physiol.*, vol. 8, article 986, Dec. 2017.

[5] M. Paci, R.-P. Pölönen, D. Cori, *et al.* "Automatic optimization of an in silico model of human iPSC derived cardiomyocytes recapitulating calcium handling abnormalities," *Front. Physiol*., vol. 9, article 709, June, 2018.

Session
Brain and Neurological Computer Interface

Feature extraction and classification of motor imagery EEG signals for brain computer interface controlled electromechanical implants

Nikolas P. Klein[1,+], Adrian Niemann [1,+], and Klaus Brinker[1]

[1] Hamm-Lippstadt University of Applied Sciences,
Marker Allee 76-78,
D-59063 Hamm, Germany

[+] these authors contributed equally to this work

E-Mail: nikolasp.klein@gmail.com, adrian.niemann@gmx.de, klaus.brinker@hshl.de

Abstract – The physical and auditive pathways used to be the only way of controlling devices and handle communication tasks. Within the last years a new type of devices was developed, so called brain- computer interfaces. This type of devices allows a new way of interaction by skipping the detour over the stated pathways and enable a direct connection between the brain and technical systems. They use a well-known clinical investigation method, called electroencephalography (EEG), to track physiological signals directly from the user's brain. These signals need several processing steps before they can be analyzed to determine the user's intention.
Due to the high variating properties of brain signals between subjects, BCIs need to be highly personalized. To build a BCI, test data from the target subject needs to be recorded and preprocessed to remove interfering noise signals, caused by environmental or biological factors. The data is then split up into train and test data. The train data set is used to train a machine learning algorithm. In this case support vector machines and different neural nets were tested, to achieve a reliable classifier, which is then tested with the test data set. The data flow can be found in Fig.1.

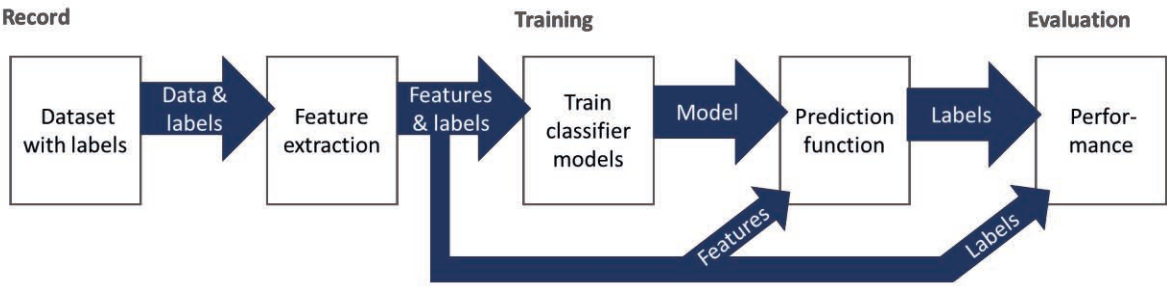

Fig.1: Model for creation process of BCIs

Test data was acquired from the test subject performing a paradigm-presenter indicated motor- imagery task (imagining movements of the right hand) using EEG. For preprocessing a notch filter at 48-52 Hz and a bandpass filter at 2-48 Hz were applied to mitigate noise from the powerlines [1] and meet specifications of a later used tool [2]. The data was then cut to trials containing one motor imagery task each. Furthermore the MARA toolbox [2] for EEGLAB [3] was used for automated artifact detection and removal. This toolbox utilizes independent components from an independent component analysis (ICA) to evaluate and remove those containing artifacts.
After the preprocessing different features were computed from the data. Those were the bandpower of different frequency bands [4], the running variance after applying a common spatial pattern (CSP) filter [5] and Hjorth features [6]. Those features were combined into sets. Each set contains one bandpower feature, one CSP processed feature, one Hjorth processed feature. A fourth feature was built by combining the bandpower feature and the CSP feature.
Each of the feature sets was then used for training and evaluating different support vector machines and neural nets.

For the support vector machines, three different types kernels were chosen, a linear function (linear), radial basis function (rbf) and a polynomial function (poly). Each of these kernels has different parameters to adjust the classifier to the given problem, which results in better classification accuracy. For the implementation of support vector machines the scikit-learn library [7] was used. It contains all three of the chosen kernels and adjustments are easy to implement. Besides setting the kernel for the standard support vector machine method on 'linear' to choose the linear kernel, the library includes an additional method for support vector machines with linear kernels (LinearSVC), which was tested as well.
Two different kinds of neural nets were considered as classification method. For time dependent information like EEG data, recurrent neural nets play an important role. In normal feed forward nets (FF), each input is processed one at a time and leads to a direct output in each node. There is no information from one step somehow transferred to the following step. In recurrent neural nets, information is processed as sequence and not as single value. In long short-term memory (LSTM) nets, a special class of recurrent neural nets, in each node an internal function evaluates its result and returns its output as another input. This feedback loop leads to an information transfer over the sequence [8].
The neural nets, which were tested had alternations within the following parameters: chosen loss functions, the optimizer, width and depth of the neural net, additional dropout layers, training batch size, activation function and number training epochs. These parameters were tested one after the other and for every parameter the one with the best result was chosen.

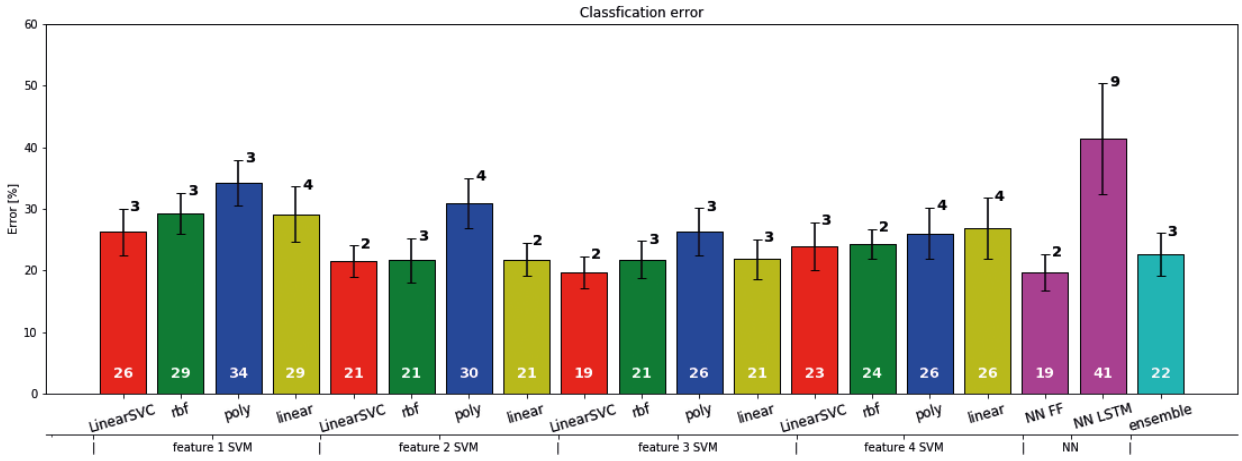

Fig.2: Results of classifiers and ensemble with feature 1 = Bandpower, feature 2 = CSP, feature 3 a combination of feature 1 and feature 2 and feature 4 the Hjorth feature

An ensemble classifier of the best support vector machine and best neural net was tested as well. The theoretical results show a maximum classification accuracy of about 80 % with a standard deviation of 3 to 5 %.

References

[1] I. Wellach, *Praxisbuch EEG: Grundlagen, Befundung, Beurteilung und differenzialdiagnostische Abgrenzung.* 2nd ed., Stuttgart: Thieme, 2015.

[2] I. Winkler, S. Haufe and M. Tangermann, “Automatic classification of artifactual ICA-components for artifact removal in EEG signals,” *Behav. Brain Funct.*, vol. 7, article 30, Aug. 2011.

[3] A. Delorme and S. Makeig, “EEGLAB: an open source toolbox for analysis of single-trial EEG dynamics including independent component analysis,” *J. Neurosci. Methods.*, vol. 134, no. 1, pp. 9–21, March 2004.

[4] Y. Wang, X. Gao, bo Hong and S. Gao, “Practical designs of brain-computer interfaces based on the modulation of EEG Rhythms,” in: B. Graimann, G. Pfurtscheller, Brendan Allison *(eds.) Brain-Computer Interfaces, The Frontiers Collection,* Berlin Heidelberg: Springer, pp. 137-154, 2010.

[5] Y. U. Khan and F. Sepulveda, “Brain-computer interface for single-trial EEG classification for wrist movement imagery using spatial filtering in the gamma band“, *IET Signal Process.*, vol. 4, no. 5, pp. 510-517, 2010.

[6] S.-H. Oh, Y.-R. Lee and H.-N. Kim, “A novel EEG feature extraction method using Hjorth parameter,” *Int. J. Electron. Electr. Eng.*, vol. 2, no. 2, pp. 106-110, 2014.

[7] F. Pedregosa *et al.*, “Scikit-learn: machine learning in Python,” *J Mach Learn Res., vol. 12, pp. 2825-2830, 2011.*

[8] P. H. Winston, *Artificial intelligence*, 3rd ed. Reading, Mass: Addison-Wesley Pub. Co, 1992.

Improvements in classification accuracy of a pre-existing P300-speller system

Adrian Niemann(1), and Klaus Brinker(1)

(1)Hamm-Lippstadt University of Applied Sciences,
Marker Allee 76-78,
D-59063 Hamm, Germany

E-Mail: adrian.niemann@gmx.de, klaus.brinker@hshl.de

Abstract – Brain-computer interfaces (BCIs) or brain-machine interfaces (BMIs) are devices that use signals generated by the brain to generate some kind of output that is transmitted by others than the normal output pathways [1], [2]. The used BCI aims to give an alternative pathway for communication which could ultimately be used by individuals that lost this ability. It therefore utilizes the brains P300 response to an unexpected stimulus. For this an 8x8 character matrix was used, flashing rows and columns in a randomized pattern. Each row and column were flashed for a fixed number of times. For the training dataset 15 flashes were used. To acquire the activity of the brains, non-invasive, easy to handle electroencephalography (EEG) has been applied. A g.tec g.Nautilus system with 8 g.SAHARA dry EEG electrodes was used.

To improve the performance of the P300-speller other than by increasing the number of spelled characters used for training classifiers the data processing before the classification was altered. The system used EEG signals that were filtered using a notch filter at 50 Hz to reduce power-line noise and different bandpass filters. Moreover, this signal was downsampled to 62.5 Hz sampling frequency. Lastly the incoming EEG data was cut into chunks, including 100 ms of data from before and 700 ms after each stimulus onset. These processed data portions were then fed into a classifier to be categorized either to include a P300 response or not. For the bandpass filtering an alteration was made. After a literature consultation the decision was made to implement a bandpass filter with a frequency band of 1 to 12 Hz [3]–[6]. This might be useful as the P300 component should lie in a frequency range of 0.6 to 2 Hz [4] and the test subject usually had a heart rate of 50 to 60 bpm whereas the cutoff frequency of 1 Hz for the filter could mitigate problems with pulse artifacts while simultaneously not attenuating the P300 response too much.

For classification there was a linear discriminant analysis (LDA) classification method already implemented in the system. This classification method has been used in several BCIs before and showed good results there [5], [7]. With an LDA a hyperplane is computed that should separate the two classes that are contained in the inserted data, as shown in Fig. 1.

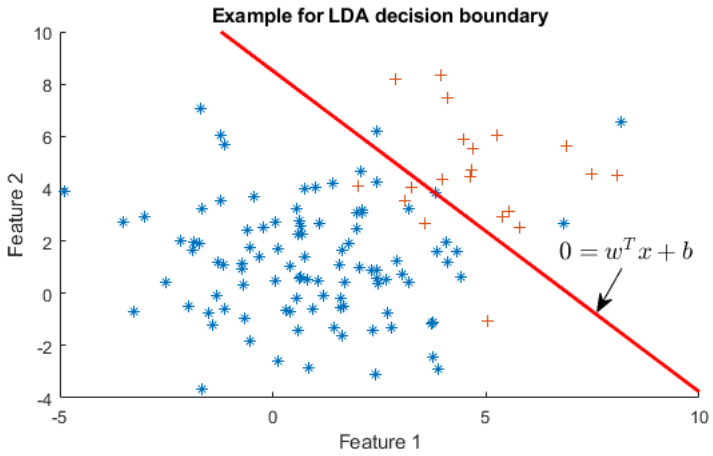

Fig.1: Example LDA decision boundary separating two classes (crosses and stars) with probabilities of occurrence matching the P300-speller experiments conducted [3], [8].

The decision can be represented by

$$y = \text{sign}(w^T x + b) \quad (1).$$

The algorithm now uses the feature vectors of the training data x_k with $k = 1, \ldots, n$ where n is the number of training data and the corresponding class labels $y_k \in -1, +1$ to estimate the elements of the bias b and the weights w. For new data that is presented to the classifier the decision is made by observing on which side of the hyperplane the feature vector is located [3], [8].

The original system used a classifier that was not personalized but rather trained on data form multiple people as a 'general' starting point. With this the system's performance varied greatly among users depending on how good their expressed brain waves would match the ones from training. For performance improvements there were now linear discriminant analysis (LDA) classifiers trained.

Using the described features classifiers were then computed using MATLAB which also optimized hyperparameters of the LDA classifiers automatically. After the training process the resulting classifiers were then tested on a test dataset and their performance was compared against the originally used 'general' classifier. As the goal was to also improve the time necessary to spell a character, there were also test datasets with a reduced number of flashes per character used. Those results are summarized in Fig. 2.

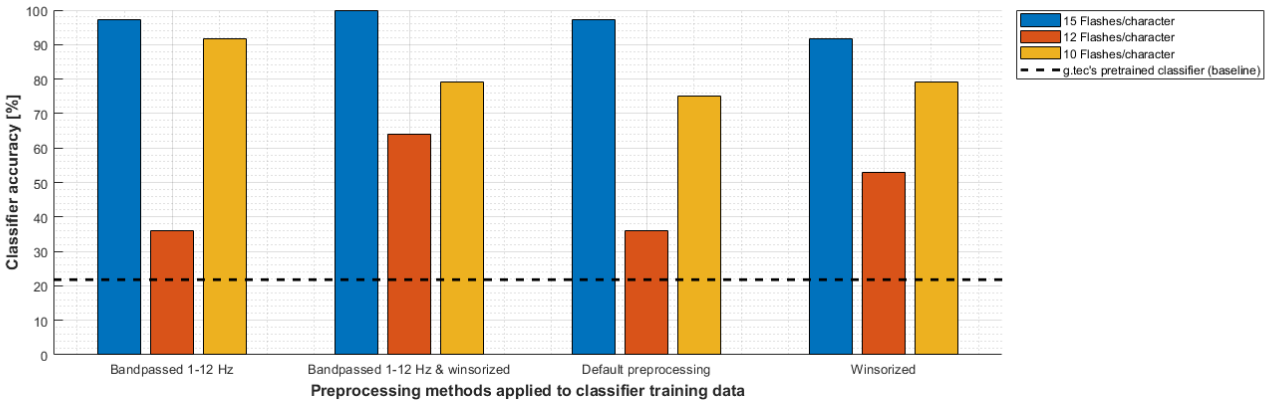

Fig.2: The accuracies of the best classifiers for character spelling for different preprocessings and flashes per character

With the personalized classifiers accuracies up to 100% using 15 flashes/character and above 90% for 10 flashes/character were achieved which is an increase in accuracy from the observed 22% using the non-personalized classifier.

References

[1] J. N. Mak, and J. R. Wolpaw, "Clinical applications of brain-computer interfaces: current state and future prospects," *IEEE Rev. Biomed. Eng.*, vol. 2, pp. 187-199, 2009.

[2] M. Witkowski, M. Cortese, M. Cempini, J. Mellinger, N. Vitiello, and S. R. Soekadar, "Enhancing brain-machine interface (BMI) control of a hand exoskeleton using electrooculography (EOG)," *J. Neuroeng. Rehabil.*, vol. 11, no. 165, Dec. 2014.

[3] X. Mao *et al.*, "Progress in EEG-based brain robot interaction systems," *Comput. Intell. Neurosci.*, vol. 2017, no. 1742862, 2017.

[4] F. E. Motlagh, and F. Ibrahim, "Developing an optimized single-trial P300-based brain computer interface system," in *International Conference for Innovation in Biomedical Engineering and Life Sciences*, vol. 56, F. Ibrahim, J. Usman, M. S. Mohktar, und M. Y. Ahmad, (eds.). Singapore: Springer Singapore, pp. 6-10, 2016.

[5] U. Hoffmann, J.-M. Vesin, T. Ebrahimi, and K. Diserens, "An efficient P300-based brain-computer interface for disabled subjects," *J. Neurosci. Methods*, vol. 167, no. 1, pp. 115-125, Jan. 2008.

[6] C. Guan, M. Thulasidas, and Jiankang Wu, "High performance P300 speller for brain-computer interface," in *IEEE Int. Workshop on Biomed. Circuits and Syst., 2004.*, Singapore, pp. 293-296, 2004.

[7] J. Jin *et al.*, "An adaptive P300-based control system," *J. Neural Eng.*, vol. 8, no. 3, article 036006, 2011.

[8] K.-R. Müller, M. Krauledat, G. Dornhege, G. Curio, and B. Blankertz, "Machine learning techniques for brain-computer interfaces," *Biomed. Tech.*, vol. 49, no. 1, pp. 11-22, 2004.

A hardware efficient implementation of a spike detection algorithm in neural closed-loop-systems

Andreas Erbslöh [(1)], Roman Burkard [(1)], Reinhard Viga [(1)] and Rainer Kokozinski [(1)(2)]

[(1)] Institute of Electronic Components and Circuits,
Faculty of Engineering, University of Duisburg-Essen,
D-47057 Duisburg, Germany

[(2)] Fraunhofer Institute of Microelectronic Circuit and Systems,
D-47057 Duisburg, Germany

E-Mail: andreas.erbsloeh@uni-due.de
Web: www.uni-due.de/ebs

Abstract – Different neurological diseases lead to a limitation/loss of physical sensory perception. Nowadays, the located troubleshooting cell tissue will be stimulated electrically to restore the sensory function e.g. by using an electronic implant. For example, the motoric deficiency of Parkinson's patients can be compensated by using a deep brain stimulator [1]. The hearing loss can be restored with a cochlear implant [2] and a retina implant enables patients blinded by Retinopathies Pigmentosa to have a visual impression [3]. One major disadvantage of these implants is that the stimulation parameters must be adjusted at runtime by the user itself or by medical staff. Therefore, the focus of the biological and medical research shifts towards a closed-loop stimulation. These systems offer the possibility of stimulating the cellular tissue of interest and while simultaneously recording the evoked response. The evaluation of the measured data can lead to new therapy approaches.

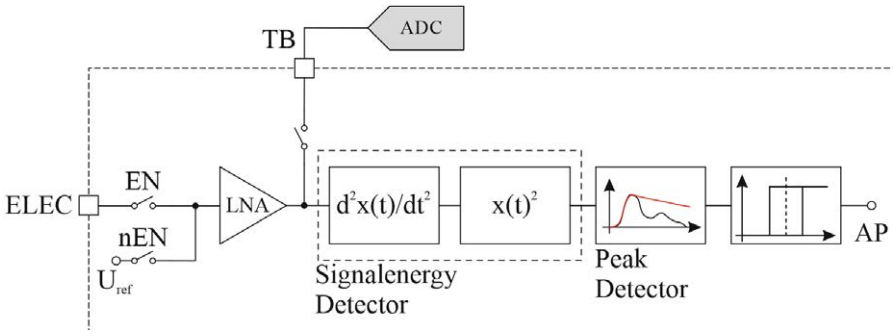

Fig.1: Block diagram of the recording module with its four stages as a monolithic integrated CMOS Closed-Loop System (from left to right: multiplexer, low noise bandwidth amplifier, spike detection algorithm, adaptive threshold detection).

This work presents the low-power hardware implementation of a fire-rate detector with an enhanced spike detection algorithm. Figure 1 shows the block diagram of one recording channel, which consists of four stages. The input multiplexer alternatively feeds the electrode signal or an internal reference voltage to a low noise amplifier (LNA) input. During the stimulation phase, the amplifier is connected to the reference voltage to prevent saturation. After an adjustable dead time, the cell response can be recorded. The LNA has a maximum gain of 32 dB. Within the -3dB bandwidth from 0.8 Hz to 4 kHz, the LNA exhibits an effective input noise of 4.32 µV and within the gain bandwidth from 0.04 Hz to 120 kHz an effective input noise of 24.96 µV. Compared to the amplitude of an action potential of 200 µV, a SNR of 18.1 dB is achieved.

$$U_{NEO}(t) = \left(\frac{dU_{in}(t)}{dt}\right)^2 - U_{in}(t) \cdot \frac{d^2U_{in}(t)}{dt^2} \quad (1)$$

$$U_{EED}(t) = \left(\frac{d^2U_{in}(t)}{dt^2}\right)^2 \quad (2)$$

To determine the fire-rate, the weak action-potentials must be filtered out of the recorded biosignals. Therefore, the non-linear-energy operator (NEO) as a spike detection algorithm is wide-spread [4].

Its origin comes from Teager's algorithm and it is a modified energy equation of a mass-spring harmonic oscillator [5] (1). In general, it is a frequency-dependent gain stage, so that the energy of an action potential can be seperated from the local field potential. A significant disadvantage of the circuit implementation of the NEO is the high circuit complexity and the high power consumption due to the use of two multiplier stages [6]. For optimization, the algorithm is analysed using the typical time shape of an action potential. The kinematic energy part of the NEO has the most impact on the gain. As a result, the circuit complexity can be reduced to a 2nd order differentiator and a squarer (2). The last stage, consists of a comparator with an adaptive threshold detection. Its output is CMOS-logic compatible and is only high, if a spike is detected from the enhanced spike detection algorithm. The adaptive functionality is achieved by a peak detector sample and leaky hold circuit (PDSH). This output drives the input of a 10 bit digital counter allowing a maximum firing rate of 1024 spikes per second. Typical firing rates of a neuron are between 10 to 160 spikes per second [7]. Figure 2 shows the functionality of the algorithm using a transient noise simulation, in which the cell behaviour is approximated by a simplified Hodgkin-Huxley-model using a VerilogA-script. The signal U_{elec} is the recorded biosignal at the electrode, U_{EED} is the output of the spike detection and U_{APcnt} is the detected action potential of the adaptive threshold detection.

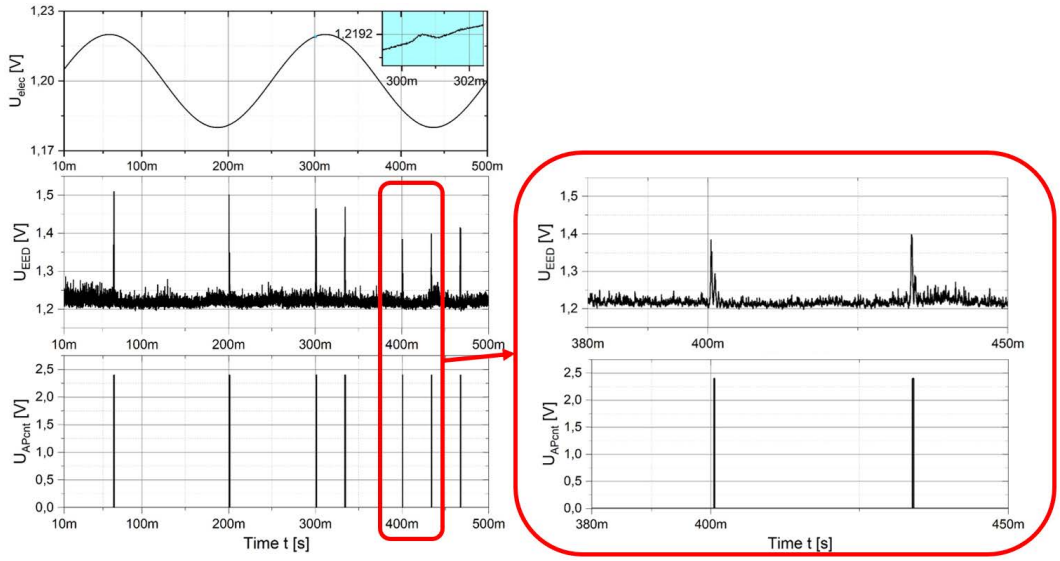

Fig.2: left: Transient noise simulation of the presented recording channel, with the electrode voltage at the input stage U_{elec}, the output of the spike detection U_{EED} and the detected spike for the digital counter U_{APcnt} – right: Enlargement of the time period from 380 ms and 450 ms.

The presented recording channel with the enhanced spike detection algorithm is integrated in an experimental closed-loop system. By cascading several of these systems, it is possible to adress a micro-electrode array of minimum eight electrodes. An integrated digital control unit enables the massively parallel processing of the recorded biosignal and carries out the stimulation with arbitrary waveforms.

References

[1] S. J. Groiss, L. Wotjecki, M. Südmeyer and A. Schnitzler, "Deep brain stimulation in Parkinson's disease", *Ther Adv Neurol. Disord.*, vol. 2, no.6, pp. 20-28, 2009.

[2] S. Maugner, C. Warren, M. Knight, M. Goorevich and E. Nel, "Clinical evaluation of the nucleus 6 cochlear implant system: performance improvements with SmartSound iQ", *Int. J. Audiol.*, vol. 53, no.8, pp. 564-576, 2014.

[3] K. Stingl, K.U. Bartz-Schmidt, H. Benav and E. Zrenner," Subretinal electronic chips can restore useful visual functions in blind retinitis pigmentosa patients", *Biomed. Tech.*, vol. 55, no.1, pp. 1-4, 2010.

[4] Y.-G. Li and Y. Massoud, „Low-power high-sensitivity spike detectors for implantable VLSI neural recording microsystems", *Analog Integrated Circuits and Signal Processing*, vol. 80, no. 3, pp. 449-457, 2014.

[5] J. F. Kaiser, "On a simple algorithm to calculate the energy of a signal", in IEEE CASS, Albuquerque, USA, 2006.

[6] A. Sarje and P. Abshire, "Low power CMOS circuit for spike detection", in IEEE SENSORS, Limerick, Ireland, 2011.

[7] J.P. Kim, H. Lee and H. Ko, "0.6 V, 116 nW neural spike acquisition IC with self-biased instrumentation amplifier and analog spike extraction", *MDPI Sensors*, vol. 18, no. 8, pp. 2460-2462, 2018.

Bayesian multi-level model to inspect relationship between socio-economic status and subjective health in 10,000 social brain

Nathania Suryoputri[1], and Danilo Bzdok[2]

[1] Faculty of Medical Engineering and Technomathematics,
FH Aachen University of Applied Sciences,
D-52428 Jülich, Germany

[2] Department of Psychiatry, Psychotherapy and Psychosomatics,
RWTH Aachen University,
D-52072 Aachen, Germany

E-Mail: nathania-amber.suryoputri@alumni.fh-aachen.de

Abstract – **Background:** Socioeconomic status (SES) is accounted to play major role in determining one's health outcome that is oftentimes represented by self-assessed health in population studies. To fall under ubiquitous social variables, SES is speculated to influence one's social interactions and their outcome. Quality and quantity of social interaction have been reported to correlate with mortality. These interrelations are presumed to accommodate an associative pathway between SES and health outcome. Preceding attempts in tracing neural underlying of human primate social interactions brought us to the social brain hypothesis, uncovering the relationship between brain size and social complexity. Previously, studies of the association between SES and social brain lead to several principles in social neuroscience such as social comparison, social-related stress as well as cognitive development and structural alterations. These foregoing studies support our investigation into the social brain.

Methods: Here we carried out Bayesian probabilistic multi-level regression aiming to expose SES' relationship with health outcome lodged in the previously extracted 36 grey-matter (GM) volumes of interest (VOI) from the social brain distributed across age from ~10,000 UK Biobank participants. The model consists of the 36 VOIs as lower-level input informed by self-assessed health and household income as well as four different social brain networks as hyper-priors. GM VOIs were extracted from ~10,000 participants by summarizing whole-brain anatomical maps guided by the topographical compartments of the social brain. Participants' structural brain was spatially smoothed with a 5mm FWHM kernel and GM measures were averaged in spheres of 5mm diameter.

Results: Our BHM managed to elaborate differences that are manifested in the social brain between socioeconomically stratified subgroups. Unalike the preceding expressed polarized relationship between lower and higher SES with health, our results emphasized the layering within both groups of SES stratifying the population by subjective health outcomes. Similar volume brain plasticity effects were displayed within higher-function and intermediate network regarding AI, SMG and cerebellum likewise in dmPFC and pMCC, regions known to be the neural basis of self-associated affective and pain representation. Positive volumetric effect was particularly demonstrated by people those having low SES and feeling healthy. In the limbic network, volumetric effect difference was displayed featuring group of lower SES separated by subjective health outcome. People feeling unhealthy showed positive volumetric effect recruiting AM and NAC, regions involved in reward and stress.

Conclusions: Our analysis of SES-related health within the social brain reviewed the common perspective of inverse relationship between SES and health outcome. We instead highlighted the social gradient characterizing their relation. SES' multilevel attribute is here represented through sets of neural basis, guiding one's perception in conducting one's social behaviour shaping health outcome. Exploring SES stratification through the perspective of social neuroscience may complement the main endeavor in comprehending a way to tackle SES-related challenge in public health.

Keywords: sMRI, social brain, Bayesian hierarchical model, socioeconomic status, health

References

[1] C. Sudlow, *et al.*, "UK biobank: an open access resource for identifying the causes of a wide range of complex diseases of middle and old age," *PLoS medicine*, vol. 12, no. 3, article e1001779, 2015.

[2] D. Alcalá-López, *et al*., "Computing the social brain connectome across systems and states," *Cereb. Cortex*, vol. 28, no. 7, pp. 2207-2232, 2017

[3] J. K. Kruschke, *Doing Bayesian Data Analysis*. London, UK: Elsevier, 2011.

[4] A. Gelman, J. B. Carlin, H. S. Stern and D. B. Rubin, *Bayesian data analysis*. Boca Raton, FL, USA: Chapman & Hall/CRC, 2014.

[5] M. G. Marmot, G. Rose, M. Shipley and P. J. Hamilton, "Employment grade and coronary heart disease in British civil servants," *J. Epidemiol. Community Health*, vol. 32, no. 4, pp. 244-249, 1978.

[6] M. G. Marmot, "Status syndrome: a challenge to medicine," *Jama*, vol. 295, no. 11, pp.1304-1307, 2006.

[7] J. P. Mackenbach, "Income inequality and population health: evidence favouring a negative correlation between income inequality and life expectancy has disappeared," *BMJ*, vol. 324, no. 7328, pp. 1-2, 2002.

[8] M. W. Kraus and D. Keltner, "Signs of socioeconomic status: A thin-slicing approach," *Psychol. Sci.*, vol. 20, no. 1, pp. 99-106, 2009.

[9] R. I. M. Dunbar and S. Shultz, "Evolution in the social brain," *Science*, vol. 317, no. 5843, pp. 1344-1347, 2007.

[10] Mattan, B.D., Kubota, J.T. and Cloutier, J., "How social status shapes person perception and evaluation: A social neuroscience perspective," *Perspect. Psychol. Sci.*, vol. 12, no. 3, pp.468-507, 2017.

[11] B. S. McEwen and P. J. Gianaros, "Central role of the brain in stress and adaptation: links to socioeconomic status, health, and disease," *Ann. N. Y. Acad. Sci.*, vol. 1186, no. 1, pp.190-222, 2010.

[12] R. Kanai and G. Rees, "The structural basis of inter-individual differences in human behaviour and cognition" *Nat. Rev. Neurosci.*, vol. 12, no. 4, pp. 231-242, 2011.

[13] N. I. Eisenberger and S. W. Cole, "Social neuroscience and health: neurophysiological mechanisms linking social ties with physical health," *Nat. Rev. Neurosci.*, vol. 15, no. 5, pp: 669-674, 2012.

[14] R. M. Sapolsky, "The influence of social hierarchy on primate health," *Science*, vol. 308, no. 5722, pp.648-652, 2005.

[15] C. F. Zink, et al., A., "Know your place: neural processing of social hierarchy in humans," *Neuron*, vol. 58, no. 2, pp. 273-283, 2008.

[16] D. Bzdok, et al., "Segregation of the human medial prefrontal cortex in social cognition," *Front. Hum. Neurosci.*, vol. 29, no. 7, article 232, 2013.

[17] Y. Luo, S. B. Eickhoff, S. Hétu and C. Feng, "Social comparison in the brain: a coordinate-based meta-analysis of functional brain imaging studies on the downward and upward comparisons," *Hum. Brain Mapp.*, vol. 39, no. 1, pp.440-458, 2018.

Listening effort and cognitive functions in cochlear implant users

Khaled Abdellatif[1], Stefan Schreitmüller[2], Martin Walger[2], and Hartmut Meister[1]

[1] Jean Uhrmacher Institute for Clinical ENT-Research,
University of Cologne,
D-50931 Cologne, Germany

[2] Clinic of Otorhinolaryngology, Head and Neck Surgery,
University of Cologne,
D-50931 Cologne, Germany

E-Mail: khaled.abdellatif@uk-koeln.de

Abstract – Cochlear implant (CI) users often report difficulties in speech understanding in noise, which in turn requires from them more concentration, attention and listening effort. Due to the fact that the cognitive capacity is generally limited [1] an increased demand level such as speech perception in noise means fewer resources are available for other tasks. This led us to the hypothesis: the lower the cognitive capacity the higher the listening effort. To test it we investigated the relationship between cognitive functions, as well as, objective and subjective listening effort in CI users.

Since speech intelligibility in noise among CI users is variable due to age at implantation, listening experience, neural survival, speech processor programs, electrode position and percentage of active electrodes [2]; a fixed speech intelligibility in noise of 80% was targeted for each participant to ensure comparable performance. Different objective cognitive tests (reading span test, trail making test) have been carried out to measure cognitive functions such as working memory capacity, processing speed and executive functions. Furthermore, listening effort has been assessed objectively with an audio/visual dual task paradigm [3] and a subjective adaptive listening effort scaling method [4].

The poster presets first results from an ongoing study and discusses possible associations between cognitive functions and objective/subjective listening effort.

Acknowledgement: Supported by the Marga-and-Walter-Boll Foundation (Ref. 210-10-13)

Keywords: Cochlear implants, listening effort, working memory capacity, speech intelligibility in noise.

References

[1] A. Wingfield, “The evolution of models of working memory and cognitive resources,” *Ear Hear*, vol. 37, no. Suppl. 1, pp. 35S-43S, 2016.

[2] D. S. Lazard *et al.*, “Pre-, per- and postoperative factors affecting performance of postlinguistically deaf adults using cochlear implants: a new conceptual model over time,” *PLoS One*, vol. 11, article no. e48739, 2012.

[3] J.-P. Gagné, J. Besser and U. Lemke, “Behavioral assessment of listening effort using a dual-task paradigm,” *Trends Hear*, vol. 21, article no. 2331216516687287, 2017.

[4] M. Krueger, M. Schulte, M. A. Zokoll, K. C. Wagener, M. Meis, T. Brand and I. Holube, ”Relation between listening effort and speech intelligibility in noise,” *Am. J. Audiol.*, vol. 26, no. 3S, pp. 378-392, 2017.

Session MRI and Tomography

Continuous measurement methods for non-invasive determination of bladder volume

Romina Möllmann(1), Wolfgang Gröting(1), Ralf Ihl(2) and Karsten Seidl(1,3)

(1) Fraunhofer Institute for Microelectronic Circuits and Systems IMS,
D-47057 Duisburg, Germany

(2) Alexianer GmbH Krefeld, Clinic for Gerontopsychiatry and Psychotherapy,
D-47805 Krefeld, Germany

(3) University of Duisburg-Essen, Department of Electronic Components and Circuits,
D-47057 Duisburg, Germany

E-Mail: romina.moellmann@ims.fraunhofer.de
Web: www.ims.fraunhofer.de

Abstract – In Germany alone, about 10 million people suffer from incontinence and are unable to control their bladder [1]. Many of these people do not dare to leave the house because they fear to suddenly feel the urge to urinate. Continuous monitoring of the bladder volume would enable these people to go to the toilet in a controlled manner without the use of continence aids. They receive a notification in time to use a bathroom. In addition, such a toilet management system could be implemented for nursing staff in order to help patients in time. Paraplegics could also determine the right time for catheterisation in order to prevent infections and to avoid stressing the bladder.

Several studies have already dealt with invasive methods for bladder volume measurement [2]. The focus of this work is on non-invasive methods to save elderly patients or patients with temporary incontinence from invasive procedures. Measurement methods based on ultrasound, impedance, radar and infrared are presented as shown in Figure 1.

Measuring the bladder volume using ultrasound is probably the best known method. The standard for inpatient urological examinations is sonography. In 1998 Petrican et al. developed one of the first permanently portable ultrasound systems to determine the bladder volume with an accuracy of 75% [3].

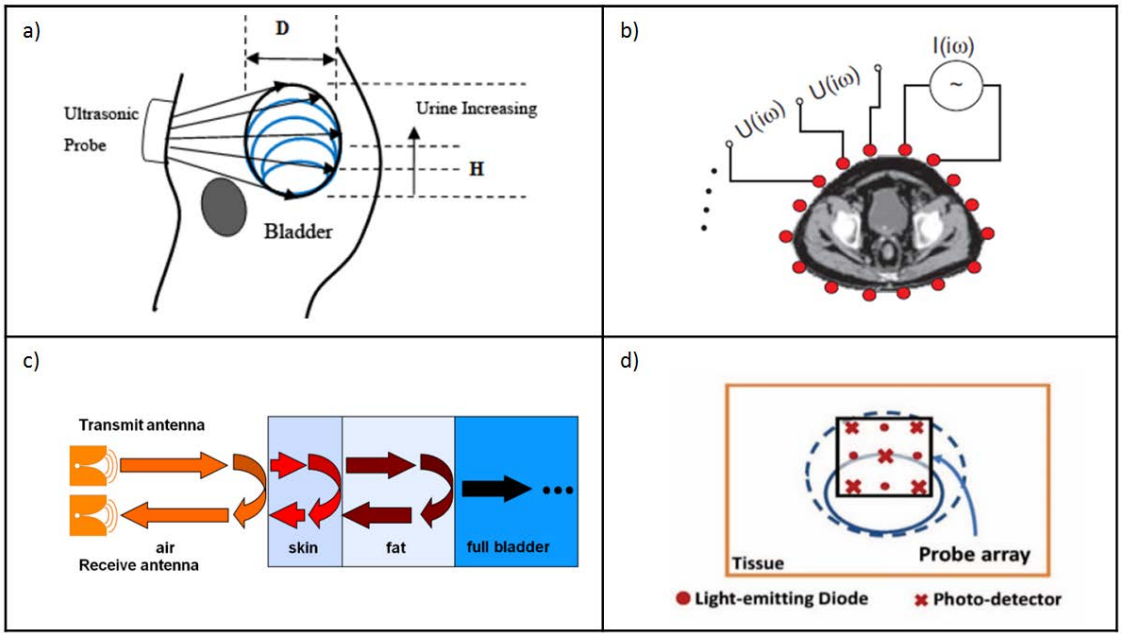

Fig.1: Overview of non-invasive measurement methods for determination of bladder volume based on: a) ultrasound [10], b) impedance [5], c) radar [7], and d) infrared [8]

B-ultrasound with 1-2.25 MHz is used predominantly, which detects the bladder walls and extrapolates the volume using the ellipsoid method. Commercial products for continuous measurement (NovioScan & Dfree) have been on the market since 2018. A disadvantage of the ultrasound method is the necessity of gel to counteract the high losses during skin transition.

Another promising measurement method is impedance tomography. This method is based on the change in global impedance, which is compared with the impedance of an empty bladder. A belt with 4 to 16 electrodes in total is used to determine the impedance. The voltage is measured at adjacent pairs of electrodes surrounding the hip while subsequently injecting a current of 5 mA at a frequency of 50 kHz between two electrodes. Denniston and Baker tested this method on dogs as early as 1975 [4]. Since 2011, Leonhardt's research group has been working on various studies and a dissertation on this topic and recently published its feasibility study [5]. In 2015, the start-up company LIR Scientific attempted to launch a bladder monitoring system using impedance tomography, but disbanded for unknown reasons. Previous methods do not allow continuous measurement, as the impedance is interfered by electromyographic signal during muscle movement. In addition, the method has a relatively large size.

Radar can also be used to measure the bladder volume. The bladder walls are detected by radar in the range of 2-7 GHz and the K-Nearest Neighbour learning algorithm to determine the volume state, i.e., full, half full and empty state. First available publications in 2010 by Li et al. show the detection of water in the bladder [6]. Irish researchers built on this in 2014 to develop a portable system [7].

The last method considered in this paper is the measurement of bladder volume using near infrared. A first available test for the detection of a full bladder was carried out in 2014 by Molavi et al. and was recently tested on pig bladders using infrared measurement [8][9]. A wavelength of 975 nm is used for the measurement, because of the high absorption point that water has at this wavelength. Different positions of diodes and detectors are conceivable.

It is obvious that the technologies are in different stages of development and that only the ultrasound method has been commercially marketed so far. However, each method has potential and can still be improved. In addition to the specific problems, there are other general challenges, such as overweight patients, the automatic determination of the Leaking Point, as well as the correct positioning without qualified personnel.

References

[1] Inkontinenz Zahlen und Fakten: https://www.insenio.de/ratgeber/ (accessed Apr.12, 2019).

[2] Arnaldo Mendez, *Bladder volume decoding from afferent neural activity.* Dissertation Polytechnique Montréal, Canada, August, 2013.

[3] P. Petrican and M. A. Sawan "Design of a miniaturized ultrasonic bladder volume monitor", *IEEE Trans. Rehabil. Eng.*, vol. 6, no. 1, pp. 66-74, 1998.

[4] J.C. Denniston and L.E. Baker, "Measurement of urinary bladder emptying using electrical impedance," *Medical and Biological Engineering*, vol.13, no. 2, pp. 305-306, March, 1975.

[5] D. Leonhäuser, C. Castelar, T. Schlebusch et al., "Evaluation of electrical impedance tomography for determination of urinary bladder volume: comparison with standard ultrasound methods in healthy volunteers," *BioMed. Eng OnLine.*, vol. 17, no. 1, p. 95, July 2018.

[6] X. Li, E. Pancera, L. Niestoruk, et al., "Performance of an ultra wideband radar for detection water accumulation in the human bladder" *Euro. Radar Conf. (EuRAD), Sept.* 30-Oct. 1, Paris, France, pp. 212-215, 2010.

[7] F. Krewer, F. Morgan, E. Jones, et al. "Development of a wearable microwave bladder monitor for the management and treatment of urinary incontinence", *SPIE Defense + Security,* Maryland, USA, 2014.

[8] B. Molavi, B. Shadgan, A.J. Macnab, et al., "Noninvasive optical monitoring of bladder filling to capacity using a wireless near infrared" *IEEE Trans. Biomed. Circuits Syst.,* vol. 8, no. 3, pp: 325-333, June, 2014.

[9] P. Raharja, A. Hamid, A.H. Hamid, et al. "Recent advances in optical imaging technologies for the detection of bladder cancer", *Photodiagnosis Photodyn. Ther.,* vol. 24, pp.192-197, 2018.

[10] H. Niu, S. Yang, C. Liu et al., "Design of an ultrasound bladder volume measurement and alarm system," *5th Inter. Conference on Bioinformatics and Biomedical Eng. (iCBBE 2011)*, May 10-12, Wuhan, China, 2011.

Design and characterization of metamaterial-based zeroth-order resonance antennas for 3T MRI

Muhamed Dedic(1), Jan Taro Svejda(1), Andreas Rennings(1), and Daniel Erni(1)

(1) General and Theoretical Electrical Engineering (ATE),
Faculty of Engineering, University of Duisburg-Essen,
and CENIDE – Center for Nanointegration Duisburg-Essen,
D-47048 Duisburg, Germany

E-Mail: muhamed.dedic@stud.uni-due.de
Web: https://www.ate.uni-due.de/index.htm

Abstract – Balanced composite right-left-handed (CRLH) metamaterial transmission lines (TL) operating at their zeroth-order resonance frequency are capable to create constant current distributions alongside them, which is directly associated to the emergence of a uniform RF magnetic field [1]. Such structures are therefore well suited for coil design in high-field magnetic resonance imaging (MRI). Based on the design of the zeroth-order resonance antenna (ZORA) for 7T MRI presented in [2], the geometry of the unit cell (UC) has been extracted and analyzed using EMPIRE XPU's [3] discrete gradient optimizer, whose ZOR frequency lies at 128 MHz, namely the operating frequency for 3T MRI. Prior to optimization, the original topology of the UC has been modified by adding a layer of FR4 while increasing the length of the UC [4]. This ensures that the effective homogeneity condition [1] is still fulfilled. During optimization, the selected geometry parameters are varied, and the scattering parameters are then simulated and compared to a set of predefined specifications. Considering the symmetry and reciprocity of the UC, the following conditions were set for this optimization:

$$|S_{22}| < -20\,\text{dB} \qquad \forall\, f \in [126\,\text{MHz}, 130\,\text{MHz}] \qquad (1)$$
$$|S_{21}| > -0.1\,\text{dB} \qquad \forall\, f \in [126\,\text{MHz}, 130\,\text{MHz}] \qquad (2)$$
$$\arg\{S_{21}\} = 0 \qquad \forall\, f \in [126\,\text{MHz}, 130\,\text{MHz}] \qquad (3)$$

Conditions (1) and (2) ensure that most of the power is transmitted from one port to the other, while minimizing reflections. Condition (3) establishes a zero crossing of the transmission phase in the given range. To simplify the design and to properly balance the unit cell, an inductor has been added connecting top and bottom copper layers. In the fabricated UC the inductor was later substituted by a lumped air coil or a short-circuited coaxial stub line [2]. Fig. 1 illustrates the final design of the UC.

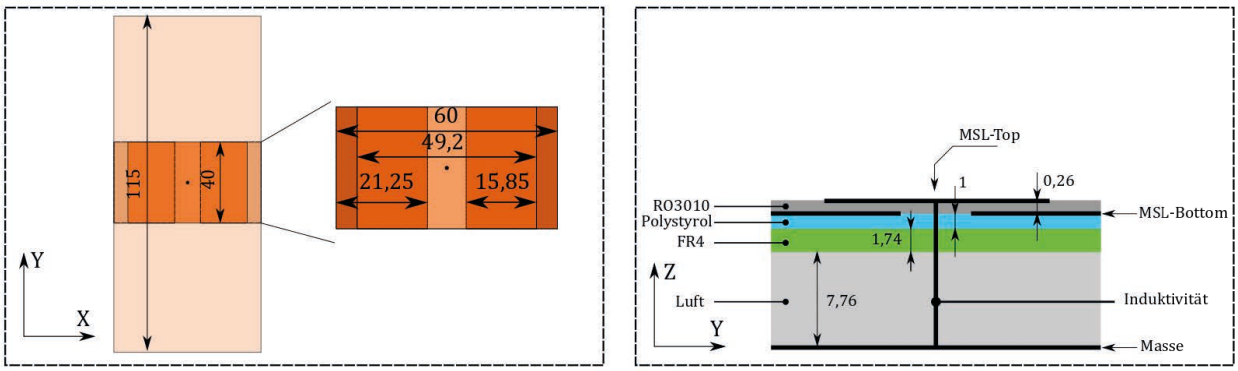

Fig.1: (left) Top view and (right) side view of the designed UC; all the measures are given in mm.

Extracting the dispersion diagram from the simulated S-parameters, the zeroth-order resonance frequency can be determined by finding the zero of the transmission phase [1]. This can be further evaluated by analyzing the Bloch impedance of the UC (cf. Fig. 3), which yields a frequency-balanced structure with a flat frequency response for its real part (i.e. a closed bandgap) [1]. The

ZORA has been setup by concatenating six unit cells and short-circuiting e.g. the terminal on one side in order to favor the series resonance with a predominantly longitudinal current flow as the operating state of the 36 cm long ZORA coil element. For validation purposes the latter has been loaded with a phantom filled with body tissue simulating liquid (BTSL) that is positioned 20 mm above the ZORA. The nearly uniform magnetic field distribution inside the phantom on a virtual plane 10 mm above its lower boundary is shown in Fig. 2. Further analyses show that the BTSL phantom's proximity does not significantly affect the resonance frequency, whilst the quality factor increases with increasing phantom distance, as shown in Fig. 3. Since ZORAs are scalable, it is possible to design differently sized antennas with similar longitudinally uniform magnetic field distributions, rendering this coil element highly suitable for various high-field MRI applications.

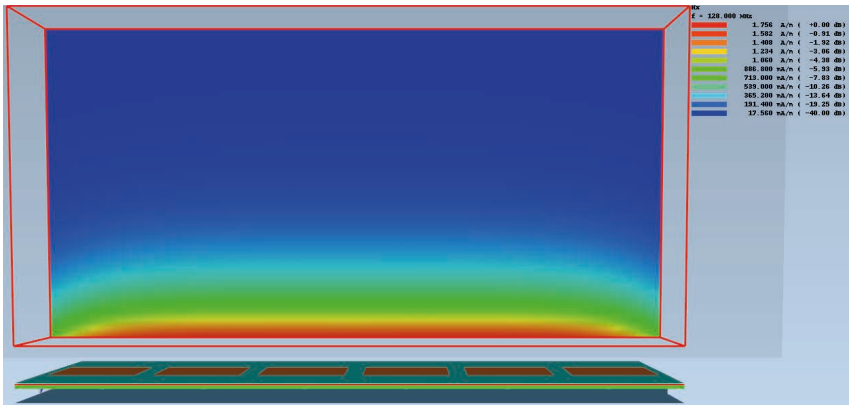

Fig.2: Virtually uniform distribution of the transversal y-component of the magnetic field 10 mm inside the BTSL phantom.

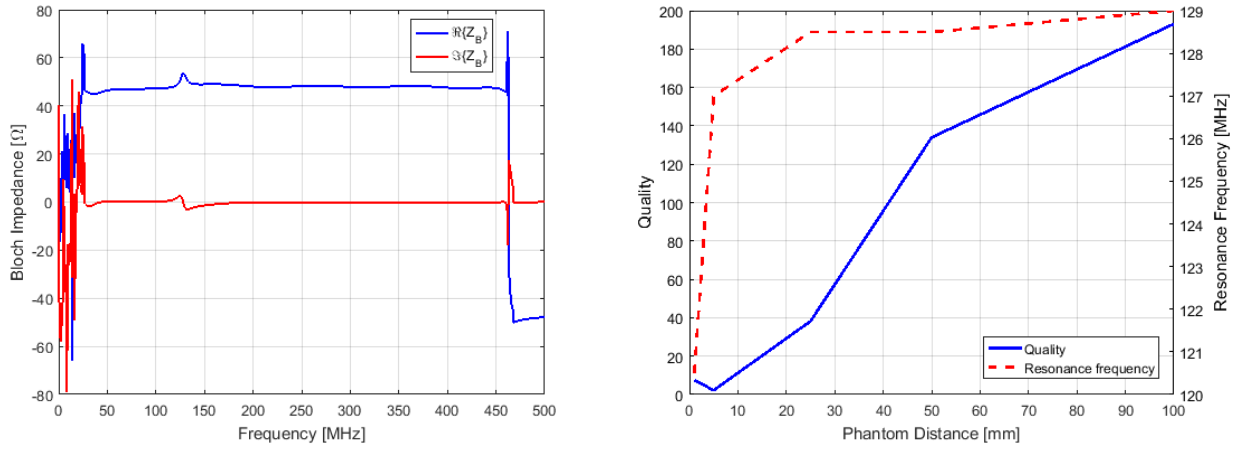

Fig.3: Spectral response of (left) the Bloch impedance, and (right) the quality factor together with the resonance frequency as a function of the distance between the ZORA coil element and the overlying BTSL phantom.

When using the Bloch impedance of the UC or an approximate resistor instead of the short-circuited termination, the CRLH-TL starts operating as a leaky wave antenna (LWA). As indicated in Fig. 3 its Bloch impedance stays nearly constant over a wide frequency range, aiming thus at ultra-broadband coil designs for e.g. multi-nuclei MRI, which is now intensely investigated in our lab.

References

[1] C. Caloz and T. Itoh, *Electromagnetic metamaterials: Transmission line theory and microwave applications – the engineering approach*. Hoboken, NJ, USA: John Wiley & Sons, 2006.

[2] C. Thiel, *Entwurf und Analyse von zeroth-order resonanten Antennen mit neuartiger Speisetechnik für die Ultra-Hochfeld-Magnetresonanztomografie*. Master thesis, University of Duisburg-Essen, April 8, 2015.

[3] The EM simulator EMPIRE XPU based on the FDTD method: http://www.empire.de/ (accessed April 22, 2019).

[4] M. Dedic, *Entwurf und Charakterisierung von metamaterial-basierten Zeroth-Order-Resonance-Spulen für die MRT bei 3 Tesla,* Bachelor thesis, University of Duisburg-Essen, Nov. 21, 2018.

The influence of CT tube current and voltage on extended Hounsfield unit values

Zehra Ese[1,2], Daniel Erni[1], and Waldemar Zylka[2]

[1] General and Theoretical Electrical Engineering (ATE),
Faculty of Engineering, University of Duisburg-Essen, and
CENIDE – Center of Nanointegration Duisburg-Essen,
D-47048 Duisburg, Germany

[2] Faculty of Electrical Engineering and Applied Natural Sciences,
Westphalian University, Campus Gelsenkirchen,
D-45897 Gelsenkirchen, Germany

E-Mail: zehra.ese@studmail.w-hs.de

Abstract – The precision of radiotherapy treatment planning (RTP) is restricted for medical implants, among others due to limitations of computed tomography (CT) imaging. Radiological CT imaging is an essential part of radiotherapy as it provides important information about the physical characteristics of the tumor and the differentiation from normal tissue. CT imaging uses Hounsfield Unit values (HU) in order to describe the attenuation of X-rays in tissue. Clinical systems use a conventional HU (CHU) scale [-1024 HU; +3071 HU], which is suited for the representation of human body tissues but is limited for high-density materials such as implants. The underestimation of implant material in RTP can lead to errors in dose calculation, which might cause an overexposure of the implant [1]. Uncontrolled irradiation of an electronic implant can lead to malfunction or even a functional loss [2]. In a previous study we have shown, that an extended HU (EHU) scale allows a proper representation of materials with a high atomic mass [3]. In this study, we quantify the influence of CT tube current and voltage on extended Hounsfield unit values.

Material and Methods: The CT systems GE LightSpeed RT (CT1), SIEMENS Somatom Definition Flash (CT2), SIEMENS Somatom Force (CT3) were used to investigate the voltage and current dependence of EHU values. Objects made from aluminium ($ED_{rel}(Al) = 2.34$), titanium ($ED_{rel}(Ti) = 3.73$), chromium ($ED_{rel}(Cr) = 5.94$) and copper ($ED_{rel}(Cu) = 7.33$) were placed in a water phantom for CT acquisition. The metallic objects were coin shaped with a diameter of $20\ \mathrm{mm}$ and a thickness of $5\ \mathrm{mm}$. All CT scans were acquired with the convolution kernel Br40 (standard). The images were reconstructed with filtered backprojection technique. The variable CT settings are shown in Tab.1.

Tab.1: CT acquisition protocols for the analysis of tube voltage (U) and current (I) dependence of EHU values.

Protocol	CT system	CT setting	
		constant	variable
(1)	CT2, CT3	$U_{1,const}$= 120 kV	$I_{2,var}$= 100 mA - 600 mA, increments of 100mA
(2)	CT1, CT2, CT3	$I_{2,const}$= 230 mA	$U_{2,var}$= 80 kV - 140 kV, increments of 20 kV

The CT images were reconstructed using extended HU scale. The EHU scale of SIEMENS CT scanners with $[-10240\ \mathrm{HU}; +30710\ \mathrm{HU}]$ is implemented using 12-bit storage, however GE use 16-bit imaging with a scale of $[-32768\ \mathrm{HU}; +32768\ \mathrm{HU}]$. In order to allow a larger HU value range at 12-bits, SIEMENS scanners increase the rescale slope from $1\ \mathrm{HU}$ to $10\ \mathrm{HU}$. In this way the standard HU scale is spread by the factor 10. For the evaluation of the HU values of the metals, a region of interest (ROI) was placed on the central part of each metal on the CT images. The mean HU value and the mean error of the ROI was quantified with a self-developed MATLAB program.

Results: The EHU values at variable current acquired with CT2 and CT3 are shown in Fig. 1 (left). The results at variable voltage for all three CT systems are shown in Fig. 1 (right). The EHU values of metal objects acquired and determined on SIEMENS CT scanners show no change at variable tube current. However, the EHU values show differences by changing tube voltage. The EHU value

of the metals decreases with increasing voltage. The mean error increase with increasing EHU value. The EHU values for all materials, regardless of voltage, result in lower values for GE scanners than for SIEMENS scanners.

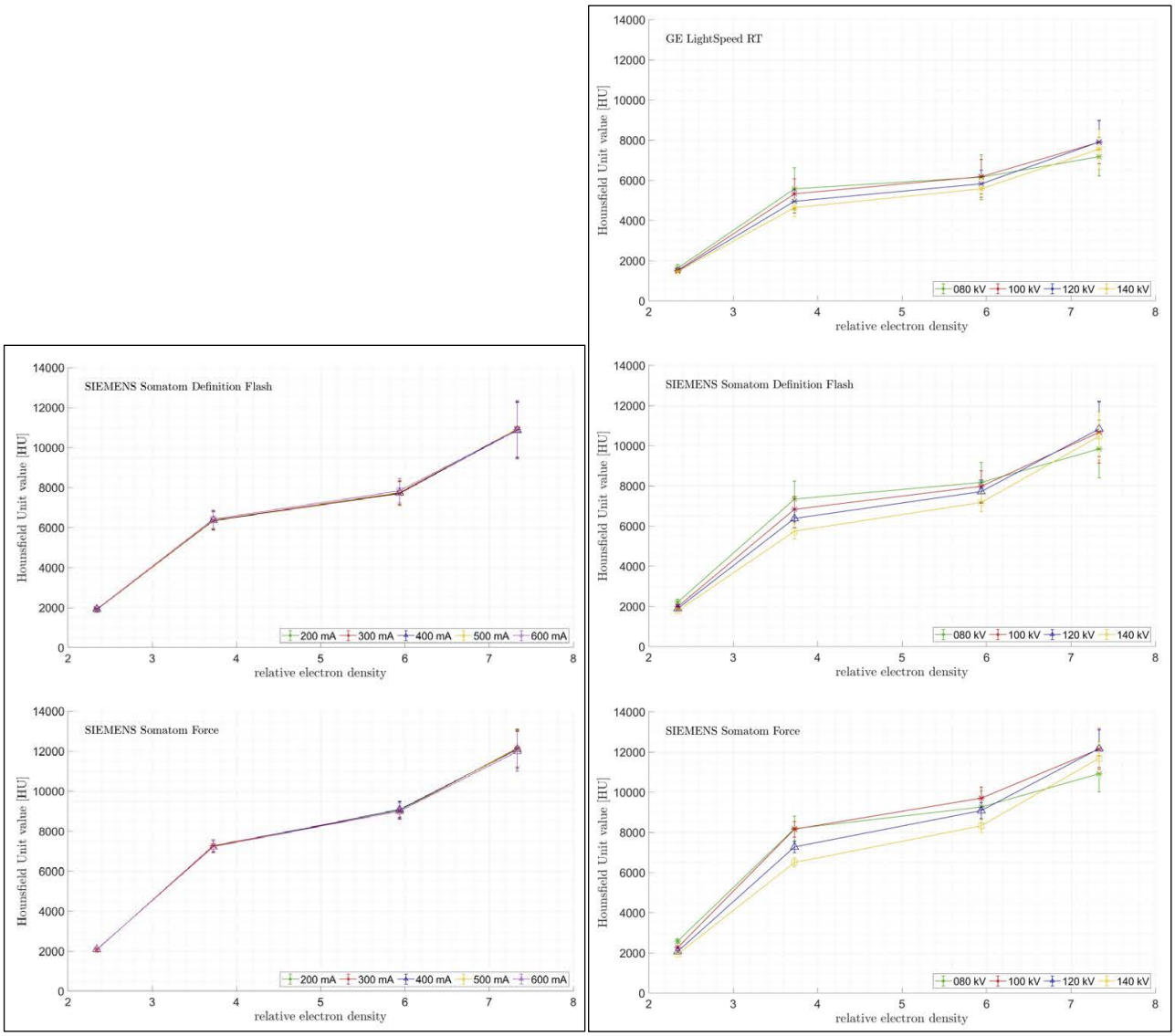

Fig.1: EHU values of metals determined on CT images acquired with variable tube current (left) and voltage (right)

Discussion and Conclusion: The EHU values are stable and independent of the tube current magnitude. However, they depend strongly on tube voltage. Small changes in HU values can lead to bigger errors in dose calculation. In order to quantify the effect of slightly changing HU values in RTP calculations, further investigations are proceeding.

References

[1] J. P. Mullins, M. P. Grams, M. G. Herman, D. H. Brinkmann, and J. A. Antolak, "Treatment planning for metals using an extended CT number scale," *J. Appl. Clin. Med. Phys.*, vol. 17, no.6, pp. 179-188, 2016

[2] M. S. Gossman, A. R. Graves-Calhoun, and J. D. Wilkinson, "Establishing radiation therapy treatment planning effects involving implantable pacemakers and implantable cardioverter-defibrillator," *J. Appl. Clin. Med. Phys.,* vol.11, no.1, pp. 33-45, 2009

[3] Z. Ese, S. Qamhiyeh, J. Kreutner, G. Schaefers, D. Erni, and W. Zylka, "CT Extended Hounsfield Unit range in radio-therapy treatment planning for patients with implantable medical devices," *World Congress on Medical Physics and Biomedical Engineering 2018*, Springer Nature Singapore Pte Ltd., IFMBE Proc. vol. 68, no. 3, pp. 599-603, 2019.

Design and first results of a phantom study on the suitability of iterative reconstruction for lung-cancer screening with low-dose computer tomography

Britta König[1,4], Nika Guberina[2], Hilmar Kühl[1,3], and Waldemar Zylka[4]

[1] Faculty of Medicine, University of Duisburg-Essen,
D-47057 Duisburg

[2] Institute for Diagnostic and Interventional Radiology and Neuroradiology,
University Hospital Essen,
D-45122 Essen, Germany

[3] Clinic for Radiology, St. Bernhard-Hospital Kamp-Lintfort GmbH,
D-47475 Kamp-Lintfort, Germany

[4] Faculty of Electrical Engineering and Applied Natural Sciences,
Westphalian University, Campus Gelsenkirchen,
D-45894 Gelsenkirchen, Germany

E-Mail: britta.koenig@stud.uni-due.de

Abstract: – We investigated computer tomography (CT) iterative reconstruction (IR) algorithms, specifically the impact of their statistical and model-based strength on image quality in low-dose lung screening CT protocols in comparison to filtered back projection (FBP). In a phantom study, we probed whether statistical, model-based IR in conjunction with low-dose, and ultra-low-dose protocols are suitable for lung-cancer screening. Preliminary results show that the strength of the IR algorithm in conjunction with a suitable convolution kernel is an indispensable alternative to FBP and may therefore be suitable for lung-tumor screening.

Introduction: Our research relates to previous studies, e.g. Lung-Cancer-Screening-Trial (NLST), 2011, conducted in USA. The trial shows that the low-dose computer tomography (LDCT) screening procedure could reduce the relative risk of lung cancer death in the risk group by 20%, which corresponds to an absolute risk reduction of 0.3% [1].

Material and Methods: Artificial lung nodules shaped as spheres with diameter d=8/10/12mm and made from material with calibrated Hounsfield Units, HU=-690/-50/+100HU, were attached on marked positions in the lung structure of the anthropomorphic LUNGMAN chest phantom PH-1 R16511 [2]. Additionally, two spherical targets with d=3/5mm, +100HU, were inserted. Distinguished radiologists selected nodule positions. The setup was scanned on Somatom Force CT Scanner (Siemens Healthineers, Erlangen, Germany) using following protocols: (i) standard high contrast (SHC; 120kV/dose modulation), (ii) low-dose (LD; 120kV/40mAs), and (iii) ultra-low-dose (ULD; 120kV/20mAs). For reconstruction, for each of three kernels (BL57; standard for lung node detection/ BR32; soft kernel/ BR69; hard kernel) FBP and the IR algorithm ADMIRE in three different strength levels (S1/S3/S5) were used [3]. Volume CT dose index CTDIvol and dose-length product DLP were recorded and the effective dose calculated. Currently, radiologists extensively review all image series in terms of lung nodules. They assess subjective image quality using a 6-point Likert scale, HU value, diameter of the largest and the smallest target, and signal- and contrast-to-noise ratios.

Results: For spherical targets CTDIvol was 2,99mGy (-70,1%) for SHC, 2,65mGy for LD (-73,5%) and 1,31mGy for ULD (-86,9%). Considering spicules, CTDIvol was 3,01mGy (-69,9%) for SHC, 2,65mGy for LD (-73,5%) and 1,31mGy for ULD (-86,9%). The drop of CTDIvol compared to the diagnostic reference value for chest CT (10mGy) issued by the Federal Office for Radiation Protection, Germany, is given in parentheses [4]. The associated probability calculated for all protocols using Student's t-Test (paired, one sided) was $p<0{,}00001$.

Preliminary results of the Likert scale assessment are presented in Fig. 1. The radiologist rated the

perceptibility of the spherical lung nodes (Fig.1: (a)-(c)) for the standard kernel BL57 with "good/moderate", for the soft kernel BR32 with "moderate/sufficient", and for the hard kernel BR69 with "good/moderate". FBP was graded with the highest occurring perceptibility for each kernel. The grade "sufficient" occurred for the kernel B32 with IR strength S1-S5 at least once and most often in conjunction with ULD, for the hard kernel BR69 only once for SHC with IR strength S5.
In general, the subjective analysis of the artificial lung nodes shaped as spheres for BL57 and BR69 was assessed similarly. However, there was a noticeably worse assessment for soft kernel BR32. The ratings "excellent" and "unacceptable" were not assigned in any case.

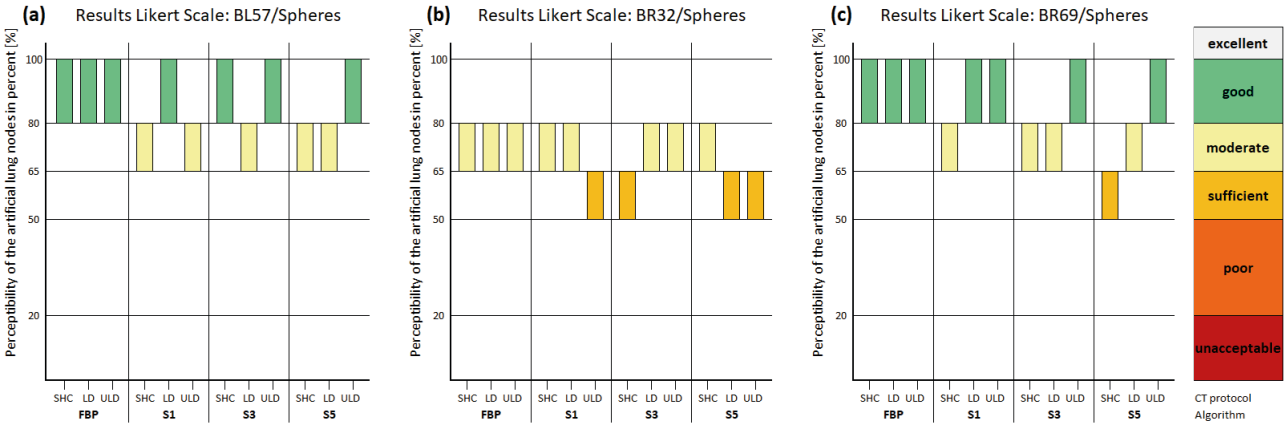

Fig.1: Results of subjective image quality analysis using the 6-point Likert Scale for the perceptibility of lung nodes: The setup with spheres is displayed in (a)-(c) for the reconstruction kernels BL57 (standard), BR32 (soft), and BR69 (hard). The horizontal axis shows the reconstruction algorithm type FBP and IR with the strength S1, S3, S5 in varying scan protocols SHC/LD/ULD. On the vertical axis the perceptibility of artificial lung nodes in percent is plotted. The percentages are presented in six colored categories on the right side of the graph.

Conclusion: The preliminary evaluation of objective and subjective quality parameters shows that the LD and ULD protocols in combination with IR enable high-quality detection of lung nodes. A first overview of the subjective analysis of a further setup with artificial spicules suggests that the perceptibility ratings for the algorithms are similar for the various kernels. Additional data is expected for the assessment of outliers in subjective evaluation and statistical analysis of an interprotocol comparison. In terms of dose reduction and subjective image quality, our preliminary results show that the medium to high strength IR algorithm in conjunction with a standard convolution kernel for lung node detection is an indispensable alternative to FBP and may therefore be suitable for lung tumor screening.

References

[1] National Lung Screening Trial Research Team, D. R. Aberle et al., "The National Lung Screening Trial: Overview and Study Design," *Radiology*, vol. 258, no. 1, pp. 243-253, January 2011.

[2] Kyoto Kagaku CO., LTD, PH1 Multipurpose Chest Phantom N1 "Lungman", https://www.kyotokagaku.com/products/detail03/ph-1.html (accessed April 8, 2019).

[3] Siemens Healthineers, ADMIRE- Advanced Modeled Iterative Reconstruction, 2019. https://www.healthcare.siemens.de/computed-tomography/technologies-innovations/admire (accessed April 25, 2019).

[4] Bundesamt für Strahlenschutz, Bekanntmachung der aktualisierten diagnostischen Referenzwerte, http://www.bfs.de/DE/themen/ion/anwendung-medizin/diagnostik/referenzwerte/referenzwerte_node.html (accessed Sept. 25,.2018).

Establishment of a 4-Alternative-Forced-Choice test to evaluate the radiological performance of iterative reconstruction in computer tomography images

Hoai Thu Nguyen [(1)], Britta König [(1,2)], and Waldemar Zylka [(1)]

[(1)] Faculty of Electric Engineering and Applied Natural Sciences,
Westphalian University, Campus Gelsenkirchen,
D-45897 Gelsenkirchen, Germany

[(2)] Faculty of Medicine,
University of Duisburg-Essen,
D-45141 Essen, Germany

E-Mail: Hoai.T.Nguyen@studmail.w-hs.de

Abstract – This paper reports about the establishment of a 4-Alternative-Forced-Choice test (4-AFC) for the evaluation of the fidelity of iterative reconstruction (IR) in computer tomography (CT) images. High image quality is essential for the assessment by a radiologist. However, when reducing dose the reconstruction by the filtered back projection (FBP) method degrades image quality and, thus, lowers diagnostic performance of the radiological reader. As an alternative, IR, which can be chosen in different strength, promises to outperform FBP. Lung phantoms with artificial lung nodes are scanned and the images are reconstructed using FBP and IR at various strength. A 4-AFC test has been developed to check if and how the strength of the IR algorithm influences the diagnosis.

Introduction: The subjective and objective quality parameters of CT images are a crucial component for the optimization of the radiation dose and the assessment of a radiologist [1]. For the newer CT systems, which are equipped with iterative reconstruction, the traditional physical quality parameters may not be suitable. In addition, they cannot provide a complete description of CT image quality. Therefore, the task-related CT image quality assessment with the help of a 4-AFC test has prevailed.

A systematic preliminary examination with low-dose X-ray CT, i.e. lung cancer screening with low-dose CT (LDCT) in the high-risk group of heavy smokers is controversial in Germany. Often an automatic tube current modulation is invoked to reduce the patient dose. However, when using FBP for image construction, this shows a low image quality and thus a lower diagnostic performance of the radiologist. As an alternative to FBP, IR algorithms have been developed in recent years, which can incorporate knowledge about the imaging system into the reconstruction process. Compared to the FBP, these algorithms produce an improved image quality with reduced radiation dose. Advanced Modeled Iterative Reconstruction (ADMIRE) is a newly developed method of IR algorithms [2].

For the investigation of image quality and diagnostic performance, both mathematical model observers and human observers are used as quantitative, objectifiable methods. Iterative algorithms present new challenges in the field of image quality evaluation. For radiology, the 4-AFC test can serve as a quantitative method that can evaluate the performance of observers. It is a psychophysical method mainly used in detection studies where radiologists were image observers. By testing the speed and accuracy of the choice, the performance of the observer can be evaluated, mainly for the quality of the imaging procedure [3].

In this work the 4-AFC test is divided into two different methods: The paired and the unpaired method. The paired method involves subjective analysis and statistical evaluation. With the unpaired method, a classification task (signal present/signal absent) is created from selected image sections of the image series and executed by human and model observers. Receiver Operating Characteristic (ROC) curves are used to evaluate the performance.

Methodology: CT images were acquired with a Somatom Force CT scanner [2] using following protocols: (a) standard high contrast (SHC; 120kV/51mAs), (b) low-dose (LD; 120kV/40mAs) and (c) ultra-low-dose (ULD; 120kV/20mAs). FBP and four different strengths of the IR reconstruction ADMIRE were used. For the purpose, phantom bodies with artificial lung nodes were imaged [3]. Spheres or spicules model the artificial lung nodes (diameter between 8 mm and 24 mm) which, are manufactured using a tissue-equivalent material. We use Matlab software to implement the 4-AFC test with DICOM images generated by the CT scanner.

Results: A medical image viewer was used to make all CT images anonymous [4]. The CT images are placed in four different bins named IR1, IR3, IR4, IR5 depending on the strength of the IR reconstruction used. Each bin contains 25 images. Fig. 1 displays the arrangement of the images in a 4-field-display area. To assure decorrelation, the images are displayed in a random order and at random position. For that purpose, one CT image from each bin was selected randomly by an equally distributed random number chosen from the interval [1,25]. The position of these four images in the 4-field-display area is random according to an additional random number drawn from equal distribution at the interval [1,24]. In fact, there are 24 possible permutation, i.e. combination for the arrangement in a 4-field-display area.

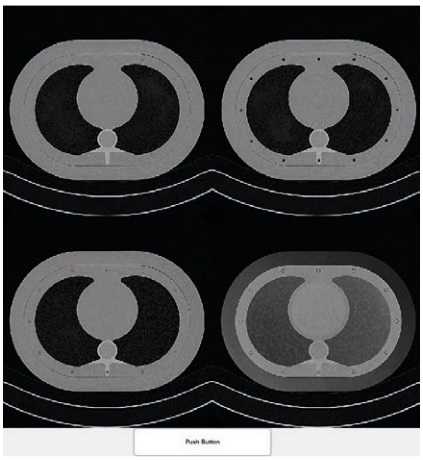

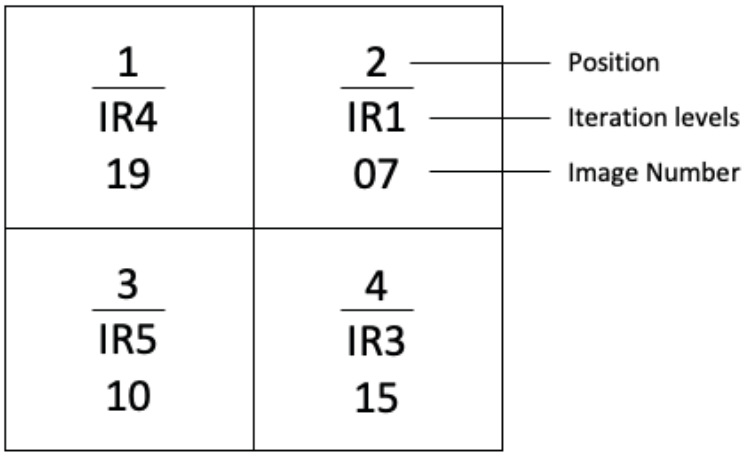

Fig.1: Left: 4-field-display area used for the 4-AFC test with the randomly selected CT images. Right: example of the assignment of the CT images randomly drawn for one particular permutation (combination 14 is shown). As described above, the numbers indicates the field position, the IR (i.e. the bins) and the number of the image.

Discussion and Conclusion: We reported on the creation of a 4-AFC test from 4+1 random numbers. The images, which are drawn from four bins with different IR levels, can take a random position determined by permutation. To this end, a fifth random number was used to arrange the images randomly in one out of 24 combinations. This allows displaying randomly chosen and randomly arranged images to the reader. In the forthcoming work, the evaluation of the diagnostic performance of the observers will be determined, e.g. by the receiver operating characteristic (ROC) curves. The results may increase the acceptance of iterative reconstruction algorithms for low-dose CT lung cancer screening and support the use of IR due to the significantly reduced radiation exposure.

References

[1] H. H. Barrett, J. Yao, J. P. Rolland and K. J. Myers: “Model observers for assessment of image quality,” *Proc. Natl. Acad. Sci. USA*., vol. 90, no. 21, pp. 9758–9765., Nov. 1993.

[2] Siemens Healthineers GmbH, Erlangen, Germany.

[3] G. Zhang, L. Cockmartin and H. Bosmans, “A four-alternative forced choice (4AFC) software for observer performance evaluation in radiology,” *SPIE Medical Imaging*, Feb. 27 - March 3, San Diego, California, United States, vol. 9787, 2016.

[4] QRM Quality Assurance in Radiology and Medicine GmbH, Möhrendorf, Germany.

[5] Horos Project, 2019.

Numerical evaluation of small animal warming potential when using a birdcage coil for 7T magnetic resonance imaging

Maíra M. Garcia [1,2], Tiago R. Oliveira [3], Daniel Papoti [3], Khallil Chaim [4], Daniel Erni [2], and Waldemar Zylka [1]

[1] Faculty of Electrical Engineering and Applied Natural Sciences, Westphalian University, D-45897, Gelsenkirchen, Germany

[2] General and Theoretical Electrical Engineering (ATE), Faculty of Engineering, University of Duisburg-Essen, and CENIDE – Center of Nanointegration Duisburg-Essen, D-47057 Duisburg, Germany

[3] Department of Biomedical Engineering, Federal University of ABC, 09606-070 São Bernardo do Campo, Brazil

[4] Department and Institute of Radiology, University of São Paulo, 05403-010 São Paulo, Brazil

E-Mail: maira.martins-garcia@stud.uni-due.de

Abstract – During magnetic resonance imaging (MRI) procedures the patients are subjected to electromagnetic (EM) waves in a radiofrequency (RF) range. The incident waves can be partially absorbed into the patient's body, due to the electromagnetic response of the patient's tissues. The excessive energy absorbed may result in tissue heating which rises concerns about patient safety [1]. The attention increases for MR applications in ultra-high fields (B_0 ≥7T), since the electrical ($\vec{E}$) and magnetic ($\vec{B}_1$) fields components demonstrate more special non-uniformity in these conditions [2]. To investigate the incident EM field distribution and its potential of tissue heating, we designed a transmit/receive linearly driven birdcage coil for small animals and performed a 3D numerical analysis to assess the temperature distribution in a phantom during MRI procedures at ultra-high field (7T). The simulated results suggest that the designed coil can be safely used to investigate small animal heads, since they will not be subjected to an excessive increase in local temperature.

Methodology: To perform the 3D numerical analysis, the commercially available software COMSOL Multiphysics 5.4 (COMSOL Inc., Sweden) was used. The designed high-pass birdcage coil for B_0=7T is made of copper, has a cylindrical shape (diameter: 10cm; height: 16.4cm), has 15 capacitors of 4.3pF and one variable capacitor (5 to 15pF) that are located at its end-rings [cf. Fig. 1a)], and its excitation is done through a single port. An EM shielding apparatus is connected to the coil in order to avoid EM interference from other hardware components of the MRI scanner. The shield has 210cm of height and 150cm diameter. A real coil was additionally constructed and some input information for the simulations was assigned using the values obtained after primary tests at the 7T MRI scanner (Siemens Healthcare, Germany) installed at PISA – imaging platform in the autopsy room, at the University of São Paulo, Brazil.
A MRI procedure was simulated using the voltage of V_0=68.7V for the coil's excitation value and assuming a gradient echo pulse sequence operating during 20 minutes. A spherical phantom with a complex geometry, positioned in the center of the coil, was created in order to represent the head of an animal subject submitted to a MRI procedure. Its geometry consists of a sphere with 7cm diameter, and in its interior part an elliptical shaped region is placed, which consists of a thin layer of bone (1mm) and brain-like tissue; the external region of the ellipse represents a muscle-like tissue [cf. Fig. 1b)] [3]. The initial temperature considered for the phantom was 37°C and the room temperature was 20°C. Finally, to analyze the potential of tissue heating, the software performed a co-simulation, due to its multiphysics capability, where the EM results served as input to calculate temperature maps [4].

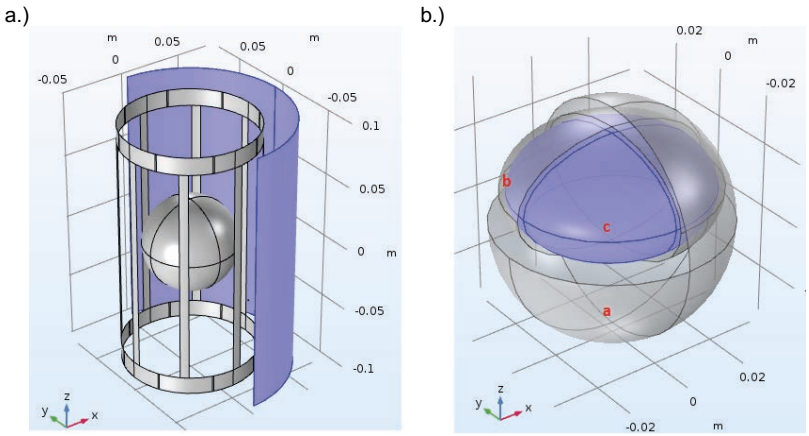

*Fig.1: a) Birdcage coil geometry, EM shield and the phantom placed in the center of the coil. b) Phantom geometry. The blue tissue (region **c**) is the brain tissue, region **b** is bone tissue equivalent and region **a** is filled with muscle.*

Results: The predictions of temperature increase after 20 minutes for the object are shown in Fig. 2, where only the axial and sagittal planes are presented.

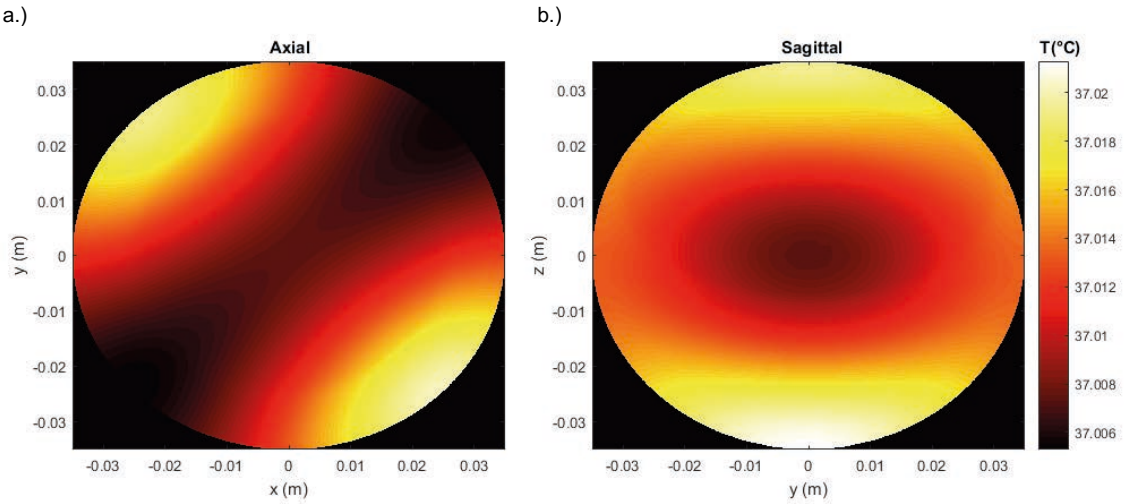

Fig.2: Temperature distribution inside the phantom. In a.) is presented the axial plane and in b.) the sagittal plane.

Discussion and Conclusion: The maximum local temperature limits on a tissue to avoid any unexpected burn are established in literature as 40°C [5]. From Fig. 2 it is possible to observe that the phantom did not suffer significant temperature increase, reaching a maximum local value of 37.02°C, which is far from the safety limit. Therefore, these results indicate that the head of a small animal would not suffer any increase in temperature above the limits, when experiencing a MRI procedure using the designed coil.

References

[1] F. Shellock, "Radiofrequency energy-induced heating during MR procedures: A review," *J. Magn. Reson. Imaging*, vol. 12, no. 1, pp. 30-36, July 2000.

[2] T. Ibrahim et al., "Analysis of B1 field profiles and SAR values for multi-strut transverse electromagnetic RF coils in high field MRI applications," *Phys. Med. Biol.*, vol. 46, no. 10, pp. 2545-2555, October 2001.

[3] S. Gabriel, R. Lau and C. Gabriel, "The dielectric properties of biological tissues: II. Measurements in the frequency range 10 Hz to 20 GHz," *Phys. Med. Biol.*, vol. 41, no. 11, pp. 2251-2269, November 1996.

[4] E. Moros, *Physics of thermal therapy – Fundamentals and clinical applications*. Boca Raton: CRC Press, 2013.

[5] T. Fiedler, M. Ladd and A. Bitz, "SAR simulations and safety," *Neuroimage*, vol. 168, pp. 33-58, March 2018.

Session Optical Analyses and Sensoring

Recognition of subjects with mild cognitive impairment (MCI) by the use of retinal arterial vessels

Jonas Zingsheim [(1)], Timo Grimmer [(2)], Marion Ortner [(2)], Christoph Schmaderer [(3)], Christine Hauser [(3)], and Konstantin Kotliar [(1)]

[(1)] Department of Medical Engineering and Technomathematics,
FH Aachen, Campus Jülich,
D-52428 Jülich, Germany

[(2)] Department of Psychiatry and Psychotherapy,
Technische Universität München,
D-80333 München, Germany

[(3)] Department of Nephrology,
Technische Universität München,
D-80333 München, Germany

E-Mail: jonas.zingsheim@alumni.fh-aachen.de
Web: www.ifb.fh-aachen.de

Abstract – Up to this day, every type of dementia, especially Alzheimer's disease dementia (ADD), is an immedicable neurodegenerative disease. Pathologically, the degeneration of the neurons is initiated in the hippocampus, wherefrom they continue to spread into further parts of the brain. Two, in this form unnaturally, occurring proteins could be autopsied in Alzheimer's disease subjects. These proteins are Amyloid-β-peptide (senile plaques) and tau-fibrils (Fig. 1) [1].

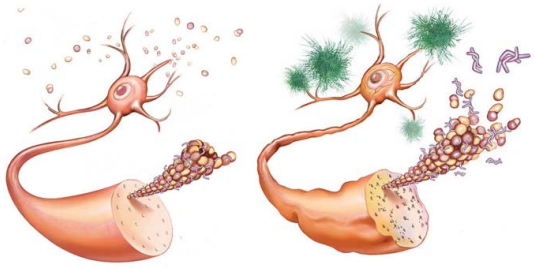

Fig.1: Healthy nerve cell without senile plaques and tau fibrils (left), Diseased nerve cell with senile plaques and tau fibrils (right), senile plaque (green), tau fibrils (purple) [2].

The embryonic linkage between the diencephalon and the retina offers a promising opportunity for an early non-invasive sensing of ADD. In collaboration with the Munich Research Center for Cognitive Disorders (TUM), this research was supplied with video recording of subjects with none-to-moderate dementia due to AD, to examined retinal blood vessels for structural and functional changes by means of a Retinal Vessel Analyzer (RVA) [3]. The obtained data additionally allows to determine spatial changes in retinal blood vessels along a chosen segment during a defined time period [4]. This chosen segment is termed “longitudinal vessel profile” (Fig.2).

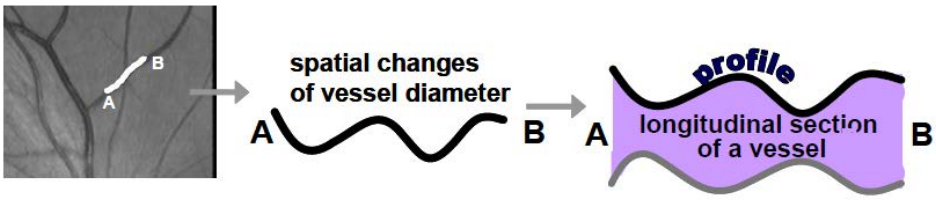

Fig.2: Definition of longitudinal vessel profile. [4]

This work deals with the intermediate group of ADD, which has already shown symptoms of mild cognitive impairment (MCI). The MCI-group can be subdivided into subjects with an AD-biomarker (MCA) and those without (MCN). Following a qualitative valuation of the measured data, the MCI-group is examined with a cognitively healthy group (HC) for local statistically significant differences by means of a parametric t- and a non-parametric U-test. It is based on the thesis [5]. The digitization of the videotapes, the preparation of the arterial longitudinal vessel profiles and the subsequent analyses of measured data are aspects of this work.

A comparison of the HC-group and the MCI-group showed a weakened result but still the same outcome as in [5]. MCI, a preliminary stage of AD-disease, already reveals changes in its dynamic functions, especially in vasodilation. Possibly caused by amyloid-β deposits on blood vessels, structural changes such as a flattened longitudinal vessel profile with smaller vessel diameters can be observed in the MCI-group (Fig. 3). The MCA-group shows, in comparison to the MCN-group, similar to the group with AD, a longitudinal vessel profile with smaller amplitudes and vessel diameters. Probably, due to the existent narrowing of the retinal vessel in MCI-subjects and the occurring hypoperfusion, consequences such as a cognitive impairment and an increased AD-risk might appear [6].

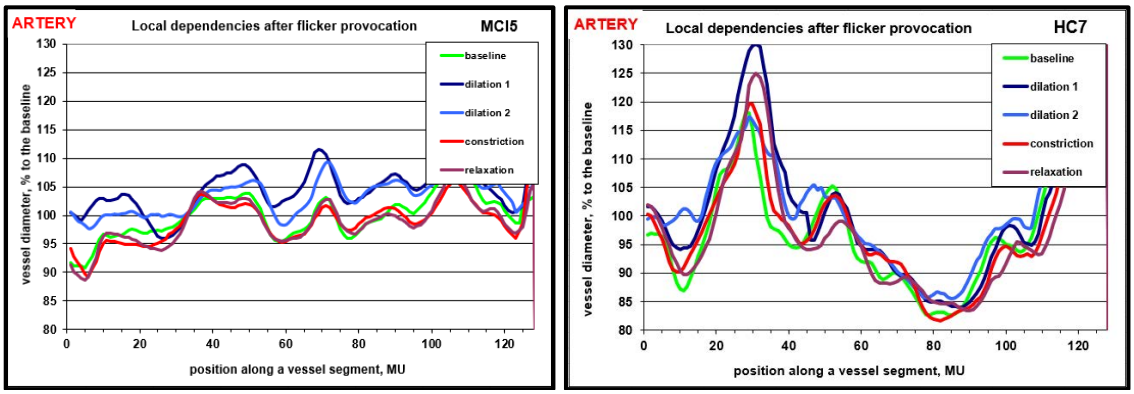

Fig.3: Left graph: Arterial local vessel diameter change [in%] to mean of baseline, mild cognitive impairment-group (MCI). Right graph: Arterial local vessel diameter change [in%] to mean of baseline, cognitively healthy-group (HC). Baseline (green), dilation 1 (dark blue), dilatation 2 (light blue), constriction (red), relaxation (dark red). [Own figure]

References

[1] S. Tsirka, A. Gualandris, D. Amaral and S. Strickland, “Excitotoxin-induced neuronal degeneration and seizure are mediated by tissue plasminogen activator,” *Nature*, vol. 377, no. 6547, pp. 340-344, September 1995.

[2] C. Leibinnes: Veränderungen im Gehirn: https://www.alzheimer-forschung.de/alzheimer/wasistalzheimer/veraenderungen-im-gehirn/ (accessed Aug. 10, 2018.)

[3] K. Kotliar, C. Hauser, M. Ortner, C. Muggenthaler, J. Diehl-Schmid, S. Angermann, A. Hapfelmeier, C. Schmaderer, and T. Grimmer, “Altered neurovascular coupling as measured by optical imaging: a biomarker for Alzheimer's disease,” *Sci. Rep.*, vol. 7, article number: 12906, October 2017.

[4] Konstantin Kotliar, *Functional in-vivo assessment and biofluidmechanical analysis of age-related and pathological microstructural changes in retinal vessels.* Dissertation TU München, München, November 26, 2008.

[5] Mahmut Bilirer, *Retinale Gefäßanalyse als Biomarker-Quelle für die Alzheimer-Erkrankung*. Bachelor thesis FH Aachen, Campus Jülich, June 2018.

[6] T. Lewis and C Trempe, *The End of Alzheimer’s: The Brain and Beyond.* San Diego: Elsevier Science, 2nd ed., 2017.

Vasomotion in retinal vessels of patients presenting post hemorrhagic hydrocephalus following subarachnoid hemorrhage

Yannik Blum[(1)], Walid Albanna[(2)], Anne Benninghaus[(3)], and Konstantin Kotliar[(1)]

[(1)] Institute for Bioengineering, Faculty of Medical Engineering and Technomathematics,
FH Aachen University of Applied Sciences,
D-52066 Aachen, Germany

[(2)] Department of Neurosurgery,
RWTH Aachen University,
D-52074 Aachen, Germany

[(3)] Chair of Medical Engineering,
Helmholtz-Institute for Biomedical Engineering, RWTH Aachen,
D-52074 Aachen, Germany

E-Mail: yannik.blum@alumni.fh-aachen.de
Web: www.ifb.fh-aachen.de

Abstract – **Background:** Clearance of blood components and fluid drainage play a crucial role in subarachnoid hemorrhage (SAH) and post hemorrhagic hydrocephalus (PHH). With the involvement of interstitial fluid (ISF) and cerebrospinal fluid (CSF), two pathways for the clearance of fluid and solutes in the brain are proposed. Starting at the level of capillaries, flow of ISF follows along the basement membranes in the walls of cerebral arteries out of the parenchyma to drain into the lymphatics and CSF [1]–[3]. Conversely, it is shown that CSF enters the parenchyma between glial and pial basement membranes of penetrating arteries [4]–[6]. Nevertheless, the involved structures and the contribution of either flow pathway to fluid balance between the subarachnoid space and interstitial space remains controversial. Low frequency oscillations in vascular tone are referred to as vasomotion and corresponding vasomotion waves are modeled as the driving force for flow of ISF out of the parenchyma [7]. Retinal vessel analysis (RVA) allows non-invasive measurement of retinal vessel vasomotion with respect to diameter changes [8]. Thus, the aim of the study is to investigate vasomotion in RVA signals of SAH and PHH patients.

Methods: The power spectral density of baseline RVA signals is analyzed in 11 patients with SAH (Group A), 9 patients with PHH (Group B) and 13 age-matched healthy controls (Group C). Spectral density of arterial and venous very low frequency (VLF) (0.02-0.06 Hz) and low frequency (LF) (0.06 - 0.15 Hz) vasomotion is compared between groups.

Results: Power of VLF observed in the artery is significantly increased in Group B compared to Group A ($p=0.041$) and Group C ($p=0.027$). Arterial ratio of VLF to LF is significantly increased for Group B compared to Group C (0.015). Group A and B show no statistically significant difference ($p=0.073$).
Conclusions: Vasomotion changes of retinal arteries is shown to be linked to the presence of PHH following SAH. Regarding the direction and relation of frequency components to the proposed pathways of fluid and solute drainage, vasomotion waves need to be further investigated.

Keywords: Retinal Vessel Analyzer (RVA), vasomotion, subarachnoid hemorrhage (SAH), post hemorrhagic hydrocephalus (PHH)

References

[1] A. W. J. Morris *et al.*, “Vascular basement membranes as pathways for the passage of fluid into and out of the brain,” *Acta Neuropathol.*, vol. 131, no. 5, pp. 725–736, March 2016.

[2] E. T. Zhang, H. K. Richards, S. Kida and R. O. Weller, “Directional and compartmentalised drainage of interstitial fluid and cerebrospinal fluid from the rat brain,” *Acta Neuropathol.*, vol. 83, no. 3, pp. 233–239, October 1992.

[3] I. Szentistvanyi, C. S. Patlak, R. A. Ellis and H. F. Cserr, “Drainage of interstitial fluid from different regions of rat brain,” *Am. J. Physiol. Physiol.*, vol. 246, no. 6, pp. 835–844, June 1984.

[4] M. L. Rennels, T. F. Gregory, O. R. Blaumanis, K. Fujimoto and P. A. Grady, “Evidence for a ‘Paravascular’ fluid circulation in the mammalian central nervous system, provided by the rapid distribution of tracer protein throughout the brain from the subarachnoid space,” *Brain Res.*, vol. 326, no. 1, pp. 47–63, May 1985.

[5] J. J. Iliff *et al.*, “A Paravascular Pathway Facilitates CSF Flow Through the Brain Parenchyma and the Clearance of Interstitial Solutes, Including Amyloid β,” *Am. J. Hypertens.*, vol. 4, no. 147, pp. 1–21, August 2012.

[6] G. Ringstad *et al.*, “Brain-wide glymphatic enhancement and clearance in humans assessed with MRI,” *JCI Insight*, vol. 3, no. 13, pp. 1–16, July 2018.

[7] R. Aldea, R. O. Weller, D. M. Wilcock, R. O. Carare and G. Richardson, “Cerebrovascular Smooth Muscle Cells as the Drivers of Intramural Periarterial Drainage of the Brain,” *Front. Aging Neurosci.*, vol. 11, no. 1, pp. 1–17, January 2019.

[8] S. Rieger, S. Klee and D. Baumgarten, “Experimental characterization and correlation of mayer waves in retinal vessel diameter and arterial blood pressure,” *Front. Physiol.*, vol. 9, no. 892, pp. 1–12, July 2018.

Utilization of fluorescence spectroscopy and neural networks in clinical analysis

Fouad Azar, Ilya Digel

Institute for Bioengineering, Faculty of Medical Engineering and Applied Mathematics,
FH Aachen University of Applied Sciences,
52428 Jülich, Germany

E-Mail: fouad.azar@alumni.fh-aachen.de, digel@fh-aachen.de

Abstract – Fluorescence topography of human urine in combination with learning algorithms can provide a variant pattern recognition method in analytical clinical chemistry and, eventually, diagnosis [1].

Fluorescent characteristics of a given solution provides not only a qualitatively unique "picture" (also known as Emission-Excitation Matrix or EEM) of the solute, which can be used to classify said solute, but also quantitative values, such as: concentration, pH, temperature and specific gravity.

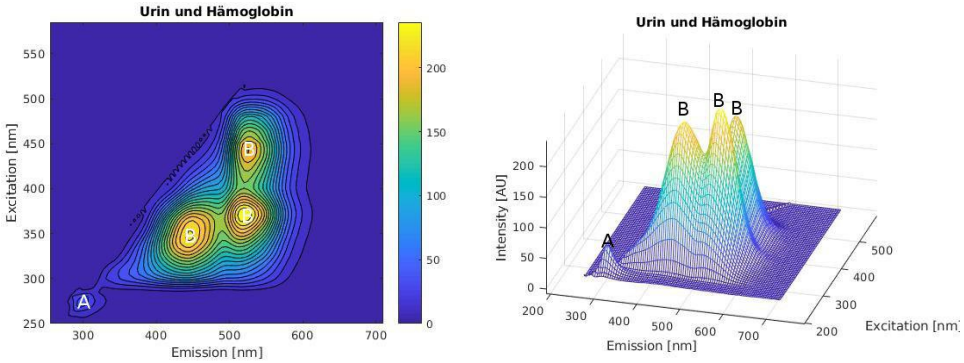

Fig.1: Fluorospectrometric measurement of B) artificial urine with A) Hemoglobin

Using the EEMs as training data for a pattern recognition network facilitates an automated process that classifies EEMs of the solute of a given solution. However, individual excitation-emission matrices obtained by fluorescence spectroscopy are mostly unique to the dissolved organic material at a given concentration, correct signal interpretation for the mixtures represents a challenge. A multi-way signal decomposition method known as PARAFAC (Tensor Rank Decomposition) can be used to extrapolate signals generated by individual components. Using unsupervised / supervised neural networks, we were able to recognize and to measure dissolved organic compounds such as NADH, FAD and ATP from their mixture (Fig. 2).

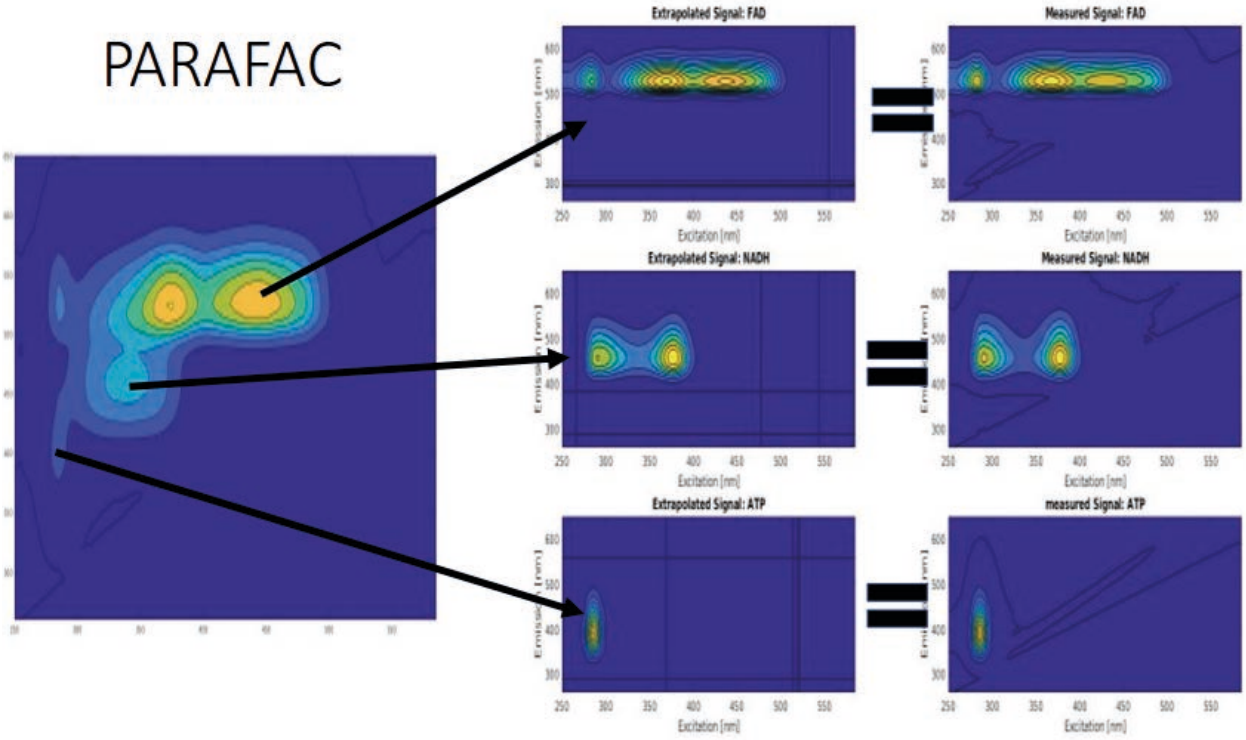

Fig.2: Application of PARAFAC to decompose a mixture ATP, NADH and FAD into the EEMs of its single constituents.

References

[1] M. J. P. Leiner, M. R. Hubmann, and O. S. Wolfbeis, "The total fluorescence of human urine," *Anal. Chim. Acta*, vol. 198, pp. 13.23, 1987.

Development of a camera-based pulse oxymeter for neonatal intensive care units

Rene Thull(1), Christian Schiffer(1), and Andreas Diewald(1)

(1) Labor für Radartechnologie und optische Systeme (LaROS),
Faculty of Electrical Engineering, Trier University of Applied Sciences,
D-54293 Trier, Germany

E-Mail: r.thull@etech.hochschule-trier.de
Web: www.hochschule-trier.de/go/laros

Abstract – The further the technique of neonatology progresses, the higher the chance of survival for premature and extremely premature infants. Such births do not always remain without lasting damage for the still very sensitive fetuses. In older age, chronic complaints such as respiratory tract problems, cognitive problems or immune system problems may occur. It is assumed that the reason for this is the stress caused by contact between the staff and the medical equipment such as the pulse oximeter and the children.

The present work (SINOPE-NEO. funded by BMBF [1]) describes an approach for systematically solving the problem of contactless pulse oximetry. In particular, the environment and physical boundary conditions within a baby incubator were considered. The aim was to develop a system which allows the implementation as well as the subsequent evaluation and successive improvements.

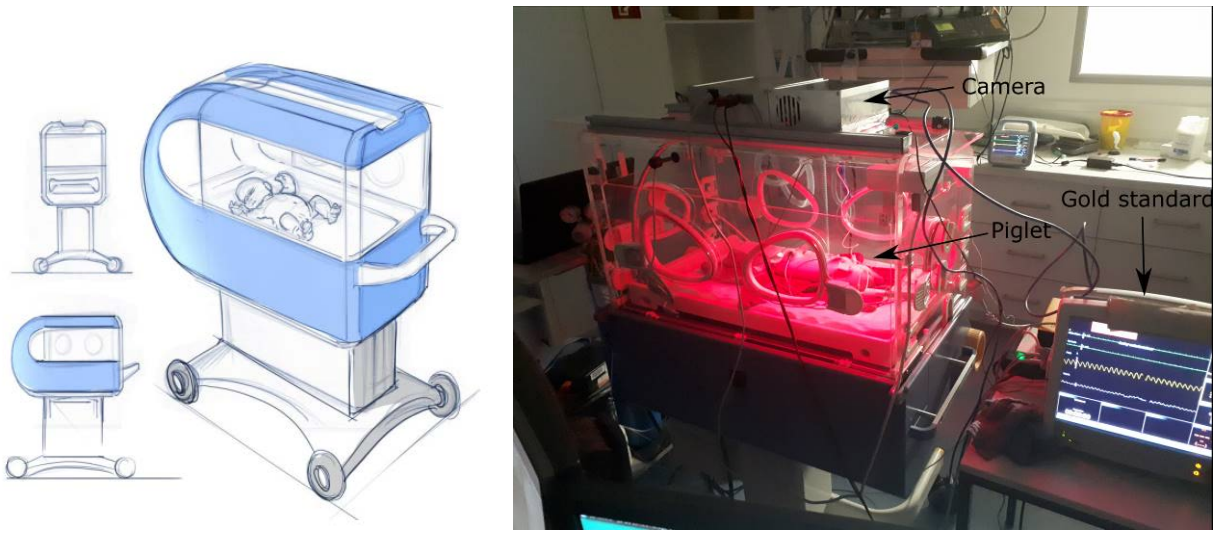

Fig.1: Left: Schematic representation of the project objective incubator. Right: Proof of Concept Incubator at a piglet measurement series at the University Hospital in Homburg.

Based on a monochrome camera from IDS with a 10-bit ADC, a sensor was developed, which works in the time multiplex procedure. For the illumination of the measuring range an illumination with flexibly controllable wavelengths of 660 nm, 810 nm and 940 nm was developed. For the control of the LED's, a microcontroller board with drivers has been designed which synchronizes with the camera. The time-division multiplex pattern of the different spectral components had to be selected in such a way that on the one hand the information density is maximized, on the other hand a compensation of the background illumination is possible and no recognizable flickering, which can lead to stress, occurs. The sensor could be integrated into an incubator commonly used in neonatology, (cf. Fig. 1).

The number of different parameters that can be changed in the system made offline data processing necessary. A graphical user interfaces was programmed in MATLAB and includes the functions Record, Analysis and Live Analysis. The Record function handles the setting, control, recording and storage of the measurement data. For a flexible application, multiple regions-of-interest (ROI), frame rate and illumination can be configured in a preview. An algorithm for determining the pulse and the oxygen saturation considering the active illumination and the camera based measurement which is based on the Beer Lambert Law described in [1], [2], [3], allows the evaluation of the recorded data.

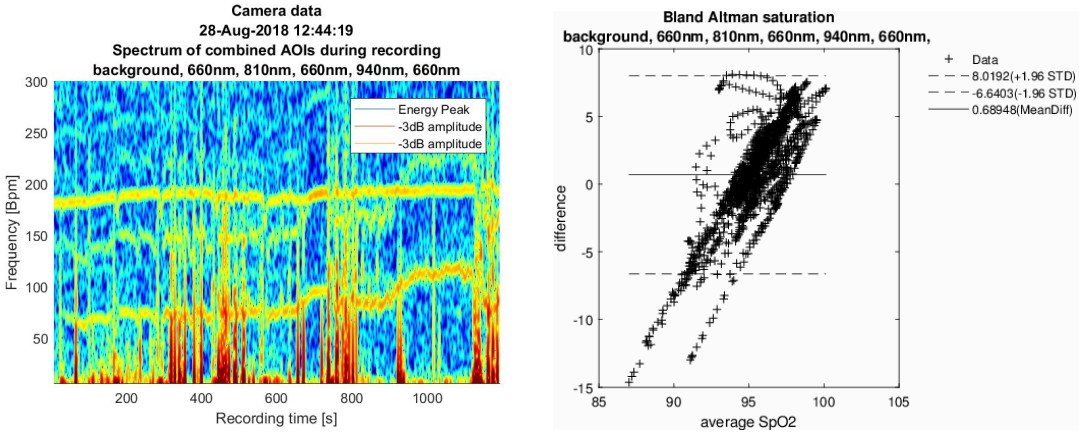

Fig. 2: Left: Cumulative spectrogram for an exemplary measurement. Right: Corresponding Bland Altman plot for the resulting saturation.

In a measurement set on minipig piglets the functionality could be proven. All wavelengths were used in the multiplex method according to λ = [660,810,660,940,660,0] nm. With a frame rate of 220 fps a measurement rate of about 36.6 Hz for all spectral components was obtained. This sampling rate was selected in order not to violate the sampling theorem and to avoid flickering. To ensure high frame rate, a lower resolution ROI had to be accepted, which was about 250² px. The evaluation of the measurements revealed important information about the problems and necessary improvements that had to be made to the system. However, the function of the sensor could be proven under good conditions for which the measurement results are shown in Fig. 2.

Acknowledgement: Funded by the Germany Federal Ministry of Education and Research (BMBF) through the KMU-Innovativ program, grant 13GW0156G.

References

[1] C. Schiffer, R. Thull und A. Diewald, „A camera based system for contactless pulse oximetry," *2nd YRA MedTech Symposium, Young Researchers Academy*, June 8-9, Mülheim a. d. Ruhr, Germany, 2017.

[2] Kenneth Gerard Humphreys, *An investigation of remote non-contact photoplethysmography and pulse oximetry*, Dissertation Maynooth National University of Ireland, Maynooth, Ireland, August 2007.

[3] Fokko Pieter Wieringa, *Pulse Oxigraphy: And other new in-depth perspectives through the near infrared window*, Dissertation Erasmus Universiteit Rotterdam, Rotterdam, 2007.

Session Application of Physical Methods

Approach for erosion processes at HF-surgery devices

Tino Morgenstern[(1)], Manuel Lange[(1)], Stephan Klöckner[(2)], and Jörg Himmel[(1)]

[(1)] Institute for measurement and sensor technology,
Hochschule Ruhr West,
D-45479 Mülheim an der Ruhr, Germany

[(2)] Olympus Surgical Technologies Europe,
D-22045 Hamburg, Germany

E-Mail: Tino.Morgenstern@hs-ruhrwest.de
Web: https://www.hochschule-ruhr-west.de

Abstract: – For surgeries of benign prostatic hyperplasia the transurethral resection is the gold standard of HF-surgeries. This surgery procedure based on monopolar systems as well as on bipolar systems. Monopolar systems were already investigated in the 1970s [1–3] and bipolar systems since the 2000s with a focus on the influence of the surgery instrument on urethral strictures [4–7]. Another topic is the material wear of the resection electrodes. A relation between measured electrical properties and the material wear was shown in [8] supplemented by electric equivalent networks for modern electrode arrangements for wear investigations [9]. In this study we present a model which describes the dependency between the electrode wear and the change of the impedance of the resection electrode.

Introduction: For surgeries of benign prostatic hyperplasia the transurethral resection is the gold standard of HF surgeries and based on monopolar and bipolar technologies. A high-frequency electric current passes through the resection electrode, the prostate tissue and the irrigation fluid. Hence a high power density is generated in tissue. Thereby the cellular structure will be destroyed and cutting or coagulating effects can be achieved. The influence of monopolar systems on the surgery procedure and complications was already investigated in the 1970s [1–3]. The investigations of bipolar systems go back to the 2000s. The research focus was to clear the influence of application of surgical instruments on urethral strictures [4–7]. Another important aspect is the wear of the resection electrode caused by the surgical process [8]. In [9], an electric equivalent network was presented for the wear investigation of modern electrode arrangements. The focus of this study is to present a model which describes the relation between the electrode wear and the change of the impedance.

Methods: The resection electrodes examined here consist of a loop used for prostate resection. The loop represents the active electrode, and the resectoscope sheath represents the neutral electrode. High current densities pass through the active electrode and lead to a plasma which surrounds the loop. The erosion process caused by a plasma is described in [10], here physical processes such as particle ejection, evaporation, oxidation and melting processes are mentioned. Applying the approach of [10] on the HF resection procedure the erosion processes can be assumed as the reason for the macroscopic as well as microscopic changes of the loop surface, which are described here by a continuous removal of small cones [Fig. 1(a)] from the loop surface. The relation between the impedance $Z(t)$ and the loop surface $A(t)$ depends on the impedance Z_0 as well as the surface A_0 in the unused state and the total time of plasma activity t.

$$\frac{Z_o}{Z(t)} = \frac{A(t)}{A_0} = \frac{n(t) \cdot A_{k1}}{A_0} \cdot \left(\frac{A_{k2}}{A_{k1}} - 1\right) + 1 \qquad (1)$$

Here $n(t)$ represents the number of cones on the loop surface, A_{k2} the lateral surface area of the cone and A_{k1} the area of the cone base. The cone base area and the loop surface are parallel and in the same plane thus the cone protrudes into the loop volume. Accordingly the impedance depends on the number of cones and the ratio between the lateral surface area and the base area of the cone. With increasing time of active plasma the erosion process will go on and the loop wire diameter decreases.

Results and discussion: The change of the impedance was measured with an impedance analyzer (Agilent 4294a). The reactance was evaluated and is shown in Fig. 1(c). The second parameter, which was evaluated, is the radius of the loop wire. Here the focus was on the smallest radius of the loop wire which was determined with an optical measurement system [blue line in Fig. 1 (b)] and equation 1 [red line in Fig. 1(b)].

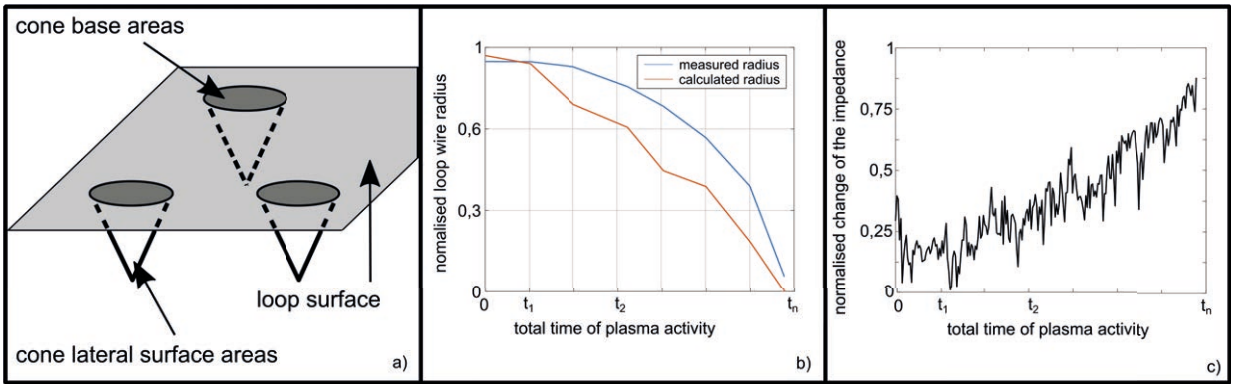

Fig.1: Model for diameter reduction (a)); Measured and calculated loop wire diameter (b)) and the resection electrode reactance (c)) in dependence of the total time of plasma activity

The measured loop wire diameter shows a negligible change of the diameter under the time t_1 with active plasma. In this time range the reactance decreases. For longer times of active plasma the loop wire diameter decreases and the impedance increases. The calculated radius shows the same behavior as the measured radius so the erosion process, modeled by cone shaped holes on the resection electrode surface, can be assumed as the reason for the changing impedance.

References

[1] J. A. Pearce, *Electrosurgery*. London: Chapman and Hall, 1986.

[2] G. Flachenecker and K. Fastenmeier, “Die transurethrale Prostataresektion mit Hochfrequenzströmen aus elektrotechnischer Sicht,” *Urologe A, vol. 15*, no. 4, pp. 167–172, 1976.

[3] Karl Fastenmeier, *Die Transurethrale Resektion mit Hochfrequenzströmen: Untersuchung und Optimierung der elektrischen Vorgänge*. Habilitation TU München, 1977.

[4] Christoph Knopf, *Methodik zur Analyse der elektrischen Feldverteilung und thermischer Vorgänge bei der bipolaren transurethralen Resektion*. Dissertation TU Chemnitz, 2014, Aachen: Shaker, 2014.

[5] P. Faul *et al.,* “Clinical and technical aspects of bipolar transurethral prostate resection,” *Scand. J. Urol. Nephrol.,* vol. 42, no. 4, pp. 318–323, 2008.

[6] P. Faul and K. Fastenmeier, “Die Rolle des Gleitmittels bei der transurethralen Elektroresektion,” *Der Urologe. Ausg. A*, vol. 47, no. 3, pp. 326–330, 2008.

[7] J. Rassweiler, D. Teber, R. Kuntz, and R. Hofmann, “Complications of transurethral resection of the prostate (TURP)--incidence, management, and prevention,” *European Urology*, vol. 50, no. 5, 969-79; discussion 980, 2006.

[8] H. Morishita, Y. Nakajima, X. Chen, M. Kimura, and S. Sato, “Electrical resistance and current leakage of appliances for transurethral resection,” (eng), *Hinyokika kiyo. Acta Urologica Japonica*, vol. 38, no. 4, pp. 413–417, 1992.

[9] T. Morgenstern, L. Gravel, S. Klöckner, O. Kanoun, and J. Himmel, “Impedance spectroscopy in HF surgery,” in *10th International Workshop on Impedance Spectroscopy · IWIS 2017*, Chemnitz, 2017.

[10] Nicolas Jeanvoine, *Plasma-material interaction and electrode degradation in high voltage ignition discharges*. Dissertation Universität des Saarlandes, Saarbrücken, 2009. Aachen: Shaker, 2011.

Diamond like carbon as a hydrophobic material for electrowetting

Semih Türk[(1)], Reinhard Viga[(1)], and Holger Vogt[(2)]

[(1)] Electronic Components and Circuits,
Department of Electrical Engineering and Information Technology, University of Duisburg-Essen,
D-47057 Duisburg, Germany

[(2)] CMOS Microsystem Technologies,
Fraunhofer Institute for Microelectronic Circuits and Systems,
D-47057 Duisburg, Germany

E-Mail: semih.tuerk@uni-due.de
Web: www.uni-due.de/ebs, www.ims.fraunhofer.de

Abstract – In many digital microfluidic applications, electrowetting is used to modify the surface tension of a fluid and to control the contact angle at the solid-gas-liquid triple point. By using electrowetting, the surface tension of a droplet is changed by an electric field between two electrodes surrounded by dielectric material. This leads to a change in the contact angle according to the Lippmann-Young equation [1]. The resulting contact angle θ is proportional to the intrinsic contact angle θ_0 and to the applied voltage V, among other things. Since the effect of electro-wetting saturates at an applied voltage of V = 40 - 50V, the applied electrical voltage must be reduced for an even greater range of contact angle modification [1]. Increasing the contact angle by microstructuring of a hydrophobic surface offer an approach [2]. This enables electrowetting application based on CMOS chips, e.g. for lab-on-a-chip applications.

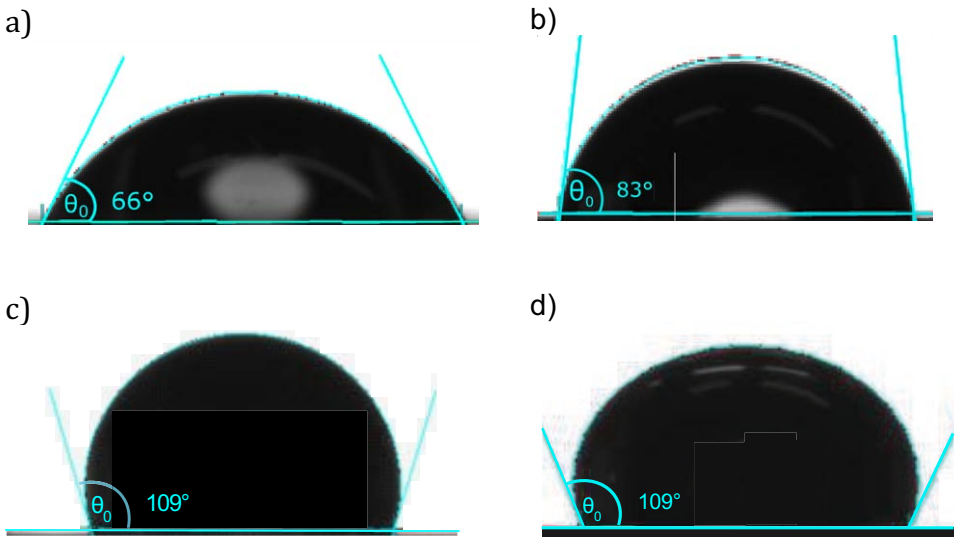

Fig.1: Measurement result of the contact angle between a water droplet and (a) DLC, (b) DLC fluorinated in SF_6-plasma, (c) DLC deposited with C_4F_8 and (d) Si deposited with C_4F_8.

In this work hydrophobic materials are investigated, which serve as a basis for super-hydrophobic surfaces. Diamond like carbon (DLC) is an often-used coating in many applications and subsequent fluorination of the DLC surface increases the hydrophobicity of the DLC layer [3]. Both C_4F_8 polymer from the passivation step of the Bosch process and SF_6 plasma were used for fluorination [4]. The intrinsic contact angle of a water droplet on the deposited hydrophobic surface

was measured (see Fig. 1). The contact angle on DLC is 66° and it is increased by fluorination in SF_6-Plasma to 83°. The deposition of C_4F_8 on DLC increases the contact angle to 109°. In addition, fluorination with C_4F_8 on Si wafers was realized to investigate the influence of C_4F_8 on hydrophobicity. In fact, C_4F_8 deposited on Si also showed a hydrophobic contact angle of 109° but has low mechanical stability.

The chemical composition of the samples was examined with the aid of EDX analysis. It could be shown that the hydrophobicity increases with increasing fluorine content of the samples (see figure 2).

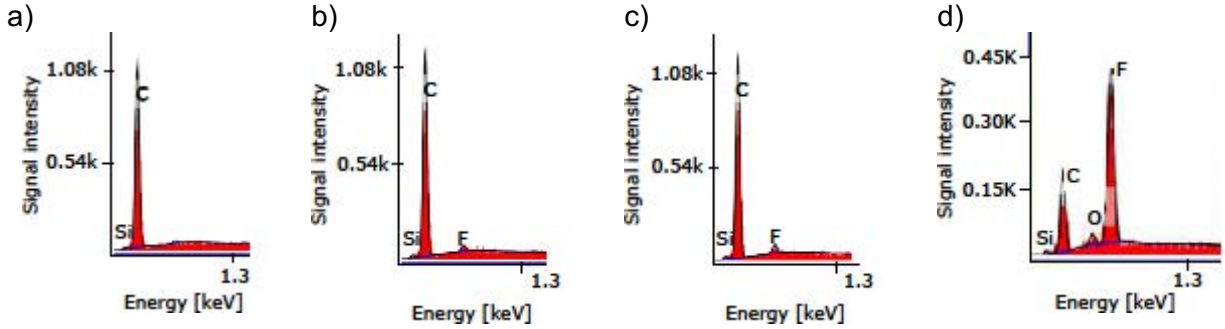

Fig.2: Measurement result of the energy dispersive X-ray spectroscopy of (a) DLC, (b) DLC fluorinated in SF_6-plasma, (c) DLC deposited with C_4F_8 and (d) Si deposited with C_4F_8.

The investigated hydrophobic layers can be optimized by microstructures to become super-hydrophobic. For this purpose, an approach for the design of the microstructures is presented. These free-standing structures have a dimension of 5x5 µm² and a height of $h = 4$ µm.

In addition to the geometry of the microstructures, the distance between adjacent microstructures also influences the wetting behavior of the droplet. A drop can be either above the microstructures with air entrapment between them (Cassie-Baxter model), or in the trenches between the microstructures (Wenzel model). The droplet adopts the energetically more favorable wetting state [2].

The resulting contact angles θ_{CB} and θ_W were analytically calculated according to the model of Cassie-Baxter and Wenzel, respectively, as functions of the distance b between adjacent microstructures. The analytical results show that both wetting states are energetically equally favorable at the critical distance b_{CR} and it is $b_{CR} = 3.11$ µm for $\theta_0 = 109°$. With decreasing distance $b < b_{CR}$ the Cassie-Baxter state becomes energetically more favorable for the drop and with increasing distance $b > b_{CR}$ the Wenzel state is energetically more favorable.

References

[1] J. Berthier, *Micro-Drops and Digital-Microfluidics.* 2nd ed., Oxford: William Andrew, 2013.

[2] B. He, N. A. Patankar and J. Lee, "Multiple equilibrium droplet shapes and design criterion for rough hydrophobic surfaces," *Langmuir*, vol. 19, no. 12, pp. 4999-5003, 2003.

[3] M. Kalin and M. Polajnar, "The wetting of steel, DLC coatings, ceramics and polymers with oils and water: The importance and correlations of surface energy, surface tension, contact angle and spreading," *Appl. Surf. Sci.*, vol. 293, pp. 97-108, 2014.

[4] S. Türk, E. Verheyen, R. Viga, S. Allani, A. Jupe and H. Vogt, "Decreasing the actuation voltage in electrowetting on dielectric with thin and micro-structured dielectric," *14th Conference on Ph.D. Research in Microelectronics and Electronics (PRIME)*, July 2-5, Prague, Czech Republic, pp. 205-208, 2018.


1 Hörsaalgebäude 00H01
2 Gerling Pavillon
3 Mensa
4 Parkplatz
Merscher Feld
Haubourdinstraße
FH Aachen Abteilung Jülich
Fachhochschule Aachen, Campus Jülich
Elektro Station
Mensa IV
Mensa-Anbau
Studentenwohnheim Solarcampus
Heinrich-Mußmann-Straße
Gerling Pavillon
Horsaalgebäude 00H01
Von-Schöfer-Ring
Solar Campus
© OpenStreetMap-

Objectives

- The aim of the YRA is to build a scientific community amongst young MedTech researchers, namely bachelor, master, and doctoral students of all types of universities (Uni & FH) in NRW.

- The aim of this YRA symposium (free of charge) is to provide an open platform for bachelor, master, and doctoral students to present either their work in progress or their final thesis in the realm of (bio-)medical engineering or in related fields such as e.g. (non-exhaustive):

  – Biomechanics, Implants, Biofluidmechanics, Microfluidics, …
  – Bioinformatics, Telemedicine, AAL, Hospital Engineering, …
  – Bioelectromagnetics, Bioelectronics, Biophysics, Medical Physics,…
  – Medical Imaging, Biosensors, Lab-on-a-Chip,…
  – Numerical Modeling, HPC, Multi-Scale Approaches, …

Paper Submission

- Submission: You are kindly invited to submit a one (up to maximal two) page abstract (Word and PDF format) until April 30th, 2019 to: info@yra-medtech.de (a prior announcement of participation is welcome).

- Format: Please use the corresponding MSWord template that is provided on the YRA MedTech website: http://www.yra-medtech.de/ (submission includes the silent consent of any (co-) authors for publication).

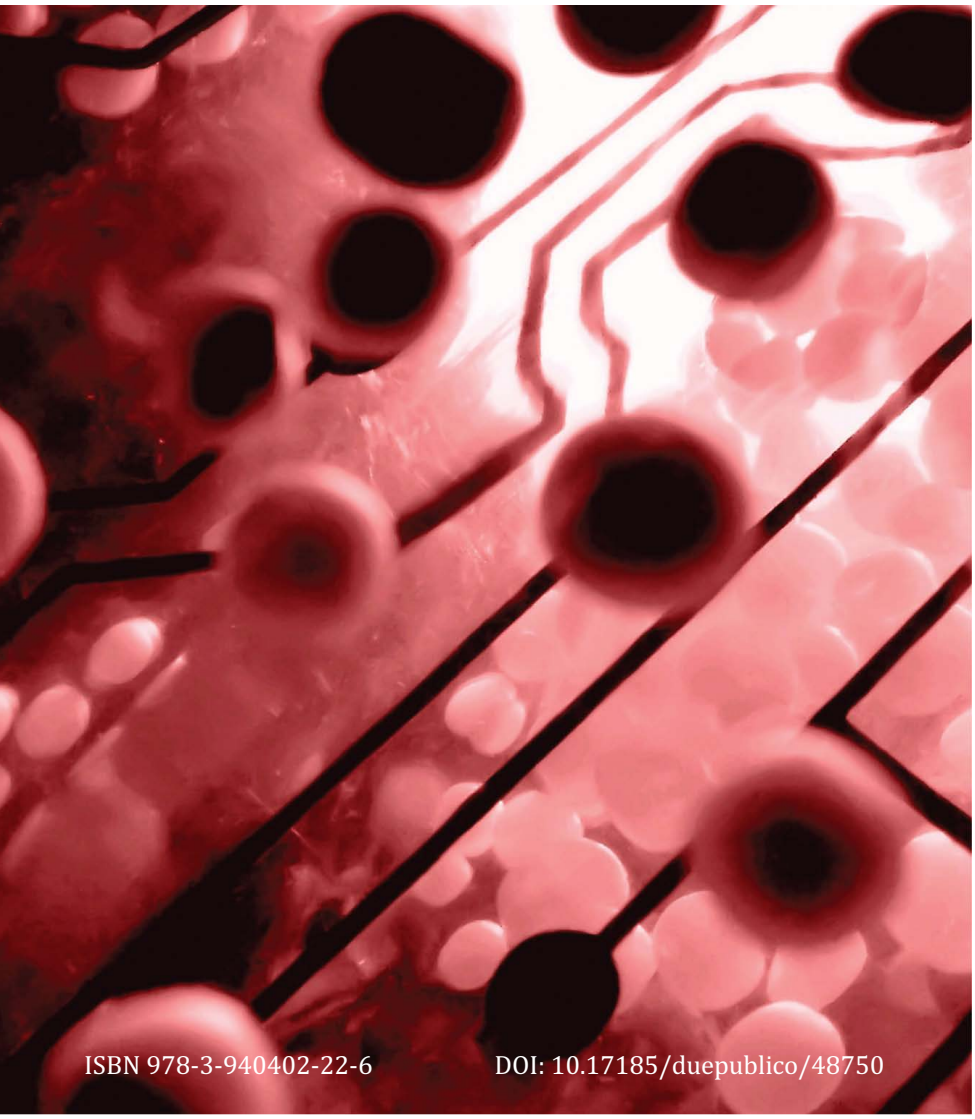

ISBN 978-3-940402-22-6 DOI: 10.17185/duepublico/48750

YRA Organizing Board

UNIVERSITÄT DUISBURG ESSEN

Prof. Dr. sc. techn. Daniel Erni
Prof. Dr.-Ing. Wojciech Kowalczyk
Prof. Dr. rer. nat. Josef Pauli
Prof. Dr. med. Joachim Fandrey

HRW HOCHSCHULE RUHR WEST UNIVERSITY OF APPLIED SCIENCES

Prof. Dr.-Ing. Jörg Himmel
Prof. Dr.-Ing. Frank Kreuder

Westfälische Hochschule

Prof. Dr. Heinrich Martin Overhoff
Prof. Dr. Waldemar Zylka

Fachhochschule Dortmund
University of Applied Sciences and Arts

Prof. Dr.-Ing. Thomas Felderhoff
Prof. Dr.-Ing. Marius Geller

FH AACHEN
UNIVERSITY OF APPLIED SCIENCES

Prof. Dr.-Ing. Manfred Staat
Prof. Dr. rer. nat. Karl Ziemons

HOCHSCHULE HAMM-LIPPSTADT

Prof. Dr.-Ing. Jürgen Trzewik
Prof. Dr. Wolfgang Kamin

Contact

Prof. Dr. sc. techn. Daniel Erni

info@yra-medtech.de
http://www.yra-medtech.de/

YRA Symposium Chairs

Prof. Dr.-Ing. Manfred Staat
Prof. Dr. rer. nat. Karl Ziemons
Prof. Dr.-Ing. habil. Konstantin Kotliar
Prof. Dr. sc. techn. Daniel Erni